Wind Tunnel Investigation of a Flexible Wing High-Lift Configuration with a Variable Camber Continuous Trailing Edge Flap Design

Nhan T. Nguyen [a]
NASA Ames Research Center, Moffett Field, CA 94035
Nathan Precup [b] and Eli Livne [c]
University of Washington, Seattle, WA 98195
James Urnes, Sr. [d]
Boeing Research & Technology, St. Louis, MO 63134
Eric Dickey [e]
Boeing Research & Technology, Huntington Beach, CA
Chester Nelson [f]
Boeing Commercial Airplanes, WA 98124
Jonathan Chiew [g]
Stanford University, Stanford, CA 94305
David L. Rodriguez [h]
Science and Technology Corporation, Moffett Field, CA 94035
Eric Ting [i] and Sonia Lebofsky[j]
Stinger Ghaffarian Technologies, Inc., Moffett Field, CA 94035

This paper presents wind tunnel experimental results of a flexible wing high-lift configuration with a variable camber continuous trailing edge flap (VCCTEF) design for drag minimization, tested at the University of Washington Aeronautical Laboratory (UWAL) in July of 2014. The objective of the high-lift test in UWAL is to assess the high-lift performance of the VCCTEF. The wing bending stiffness is tailored to achieve a wing tip deflection of about 10% of the wing semi-span at 1-g flight conditions. The VCCTEF is a multi-segment flap design having three chordwise camber segments and five spanwise flap sections for a total of 15 individual flap elements. The high-lift design includes a Variable Camber Krueger (VCK) leading edge device and an inboard high-lift trailing edge flap with a Fowler motion. Two inboard high-lift flap configurations are tested: a single-element plain flap and a three-segment cambered flap. The outboard VCCTEF is rigged at varying flap deflections of up to 30° formed by a circular arc camber and has no Fowler motion. A premature flow separation associated with the initial configuration of the VCK leading edge device, as indicated by an abrupt stall, was encountered during the initial runs. A final VCK configuration was found experimentally with a varying rigging angle from 65° at the inboard to 50° at the outboard. Wind tunnel test results indicate a $C_{L_{max}} = 2.13$ is achieved for a wing-body configuration with the single-element plain flap versus $C_{L_{max}} = 2.09$ with the cambered flap. This $C_{L_{max}}$ is close to the desired $C_{L_{max}}$ for a typical Boeing 757 landing configuration. The cambered flap achieves a L/D improvement by 6% over the single-element plain flap due to the reduced profile drag with the cambered flap. Sensitivities due to VCCTEF spanwise deflection shapes, combined Reynolds number / aeroelastic effect, and Fowler slot width were studied. Reynolds / aeroelastic and Mach number corrections

[a]NASA Ames Research Center, Research Scientist, AIAA Associate Fellow, nhan.t.nguyen@nasa.gov
[b]University of Washington Aeronautical Laboratory, Operations Manager, nprecup@u.washington.edu
[c]University of Washington, Endowed Boeing Professor of Aeronautics and Astronautics, eli@aa.washington.edu
[d]Boeing Research & Technology, Program Manager (Retired), james.m.urnes-sr@boeing.com
[e]Boeing Research & Technology, Aerodynamics Engineer, eric.d.dickey@boeing.com
[f]Boeing Commercial Airplanes, Boeing Technical Fellow, chester.p.nelson@boeing.com
[g]Stanford University, Ph.D. Candidate, Dept. of Aeronautics and Astronautics, jchiew@stanford.edu
[h]Applied Modeling and Simulation Branch, NAS Division, david.l.rodriguez@nasa.gov
[i]NASA Ames Research Center, Intelligent Systems Division, Research Engineeer, eric.b.ting@nasa.gov
[j]NASA Ames Research Center, Intelligent Systems Division, Research Engineeer, sonia.lebofsky@nasa.gov

were performed to estimate the values of $C_{L_{max}}$ at flight Reynolds and Mach numbers. The corrections result in estimated $C_{L_{max}} = 2.22$ for the plain flap and $C_{L_{max}} = 2.19$ for the cambered flap, roughly about 4% increase. An aeroelastic analysis was performed to analyze the bending deflection measurements from an optical VICON system and the torsional twist data computed from the VICON measurements. The bending deflection measurements show very good data consistency, but the computed torsional twist data exhibit high degree of scatter. The wind tunnel test confirms that the high-lift design for the VCCTEF is capable of providing high-lift performance for transport aircraft. The test results also confirm the potential drag reduction benefit for the three-segment cambered flap as compared to the plain flap.

I. Introduction

The aircraft industry has been responding to the need for energy-efficient aircraft by redesigning airframes to be aerodynamically efficient, employing light-weight materials for aircraft structures and incorporating more energy-efficient aircraft engines. Reducing airframe operational empty weight (OEW) using advanced composite materials is one of the major considerations for improving energy efficiency. Modern light-weight materials can provide less structural rigidity while maintaining sufficient load-carrying capacity. As structural flexibility increases, aeroelastic interactions with aerodynamic forces and moments can potentially degrade aerodynamic efficiency.

Under the Advanced Air Vehicles Program in the NASA Aeronautics Research Mission Directorate, the Advanced Air Transport Technology (AATT) Project is conducting multidisciplinary research to investigate advanced concepts and technologies for future aircraft systems. A NASA study entitled "Elastically Shaped Future Air Vehicle Concept" was conducted in 2010[1,2] to examine new concepts that can enable active control of wing aeroelasticity to achieve drag reduction. This study showed that highly flexible wing aerodynamic surfaces can be elastically shaped in-flight by active control of wing twist and bending deflection in order to optimize the local angles of attack of wing sections to improve aerodynamic efficiency through drag reduction during cruise and enhance lift performance during take-off and landing. One concept resulting from this study is the Variable Camber Continuous Trailing Edge Flap (VCCTEF) developed initially by NASA.[1] Initial study results indicate that, for some applications, the VCCTEF system may offer a potential pay-off in drag reduction that could provide fuel savings. In order to realize the potential benefit of drag reduction by active span-load and aeroelastic wing shaping control while meeting all other performance requirements, the approach for high lift devices needs to be considered as part of the wing shaping control strategy.

NASA and Boeing have jointly developed the VCCTEF further under a research program from 2012 to 2014.[4,5,14] This research program was built upon the initial development of the VCCTEF system for the NASA Generic Transport Model (GTM) in 2010. The resulting VCCTEF system developed under this program employs light-weight Shape Memory Alloy (SMA) technology for actuation and three separate chordwise segments shaped to provide a variable camber to the flap. This cambered flap has greater potential for drag reduction as compared to a conventional straight, plain flap. The flap is also made up of individual 2-foot spanwise sections, which enable different flap settings at each flap spanwise position. This results in the ability to actively control the wing twist shape as a function of span, resulting in a change to the wing twist to establish the best lift-to-drag ratio (L/D) at any aircraft gross weight or mission segment. Wing twist on traditional commercial transport designs is dictated by the aeroelastic deflection of a fixed "jig twist" shape applied at manufacture. The design of this jig twist is set for one cruise configuration, usually for a 50% fuel loading or mid-point on the gross weight schedule. The VCCTEF offers different wing twist settings, hence different spanwise loadings, for each gross weight condition and also different settings for climb, cruise and descent, a major factor in obtaining best L/D conditions. The second feature of VCCTEF is a continuous trailing edge flap. The individual 2-foot spanwise flap sections are connected with an elastomer transition material, so as to produce no gaps in between the spanwise sections. This continuous trailing edge flap can potentially help reduce viscous drag and airframe noise.

The VCCTEF is a multi-functional flap system envisioned to be:

- A wing shaping control device to twist the flexible wing and change the span-load distribution to reduce cruise drag throughout the flight envelope.
- A high-lift device for take-off, climb-out, let-down and final approach by using the full span cambered flap.
- A full span roll control effector in lieu of traditional ailerons using the aft section of the cambered flap.
- An aeroservoelastic (ASE) control device to compensate for reduced flutter margins of flexible wings and provide load alleviation control.

As part of the study in 2012 to 2014, two wind tunnel tests were performed in the Kirsten wind tunnel at the University of Washington Aeronautical Laboratory (UWAL) to explore the relative merits of the VCCTEF as a cruise drag reduction wing shaping control device and a high-lift device. The first test entry in August of 2013 was designed as an exploratory test to measure the drag reduction benefit of the VCCTEF. The results of this test have been reported.[7–9] The second test entry in July of 2014 was designed to assess the high-lift performance of the VCCTEF.[11] This paper reports the results of the second high-lift test entry.

II. Description of the VCCTEF System

The GTM (Generic Transport Model) represents a notional single-aisle, mid-size, 200-passenger transport aircraft generically approximating a Boeing 757, as shown in Fig. 1. The GTM had been extensively tested in the 14-foot–by-22-foot wind tunnel at NASA Langley Research Center. Thus, wind tunnel test data are available that can be used to validate computational models.

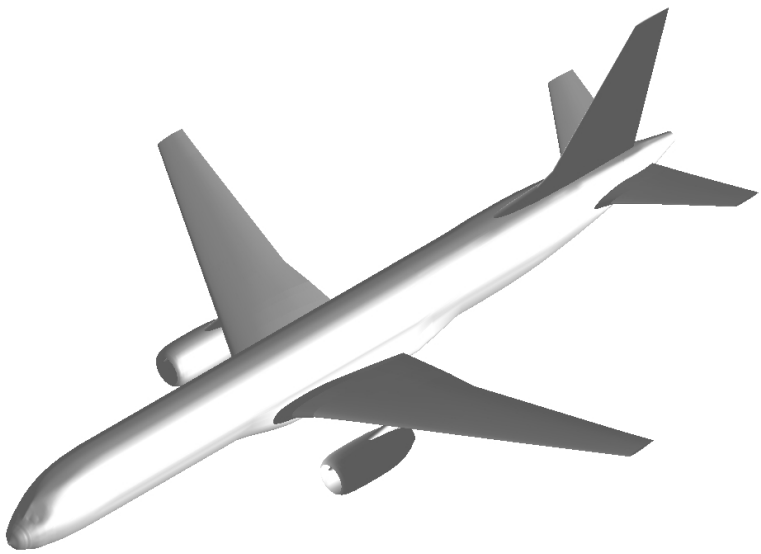

Figure 1. GTM Planform

The aircraft has a mid-cruise weight of 210,000 lbs for a typical operating load (gear up, flap up) that includes cargo, fuel, and passengers. Fuel weighs about 50,000 lbs for a range of about 3,000 nautical miles. At the design cruise condition of Mach 0.8 at 36,000 ft, the design lift coefficient is 0.51.

To assess the effectiveness of wing shaping control for modern transport aircraft, the GTM wing is modeled with a high degree of flexibility, similar to estimated flexibility distributions on state-of-the-art passenger aircraft wings. The wing bending stiffness is tailored to achieve a 10% wing tip deflection at 1-g flight conditions, which results in a bending stiffness about half that of older-generation transport wings, while the torsional stiffness is about the same. This 10% wing tip deflection is about the same as that of a modern composite high-aspect-ratio wing design in modern transport aircraft such as the Boeing 787.

The VCCTEF is divided into 14 sections attached to the outer wing and 3 sections attached to the inner wing, as shown in Fig. 2.[4] Each 24-inch section has three chordwise cambered flap segments that can be individually commanded. These cambered flaps are joined to the next section by a flexible and supported material (shown in blue) installed with the same shape as the camber and thus providing continuous trailing edge flaps throughout the wing span with no drag producing gaps.

A major goal of the program is to develop a light-weight flap control system that has a significant weight advantage as compared to current flap screw-jack actuators. Hydraulic, electric and Shape Memory Alloy (SMA) torque rod actuation were evaluated with the result that the SMA actuation has the best weight advantage. Moreover, the use of hinge line actuation eliminates the large and heavy externally mounted actuators, and permits all actuators to be interior to the wing and flap mold lines, thus contributing to the overall drag reduction goal.

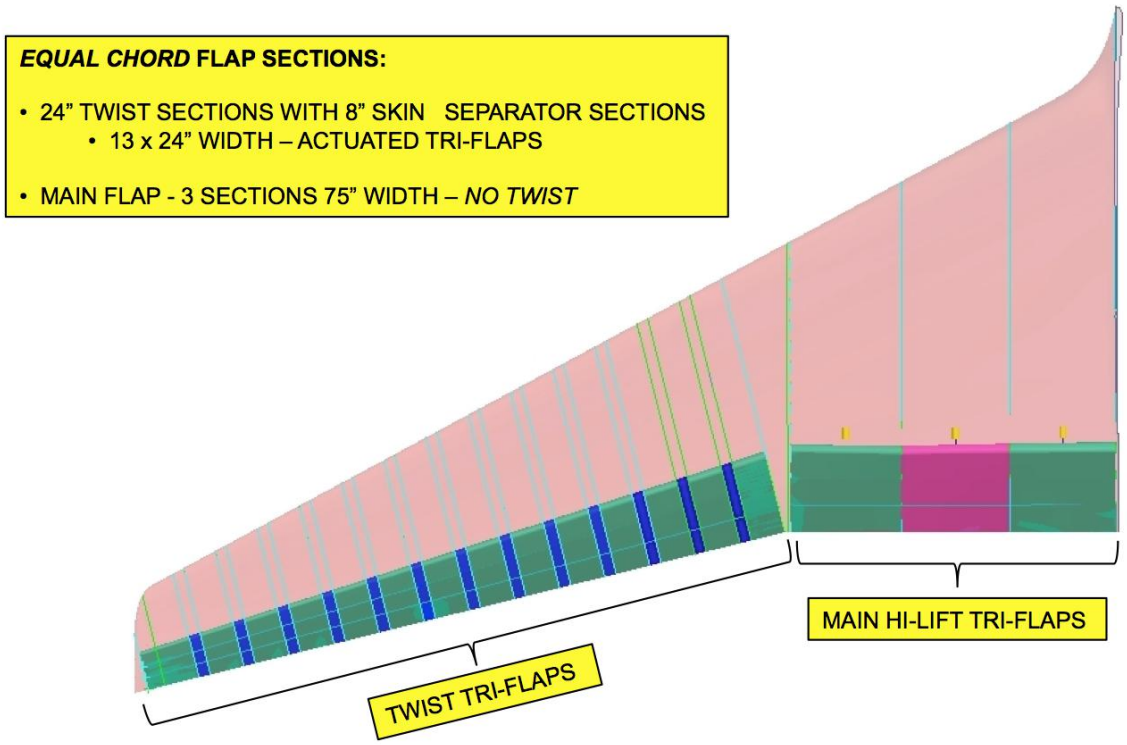

Figure 2. Wing Configured with the Variable Camber Continuous Trailing Edge Flap

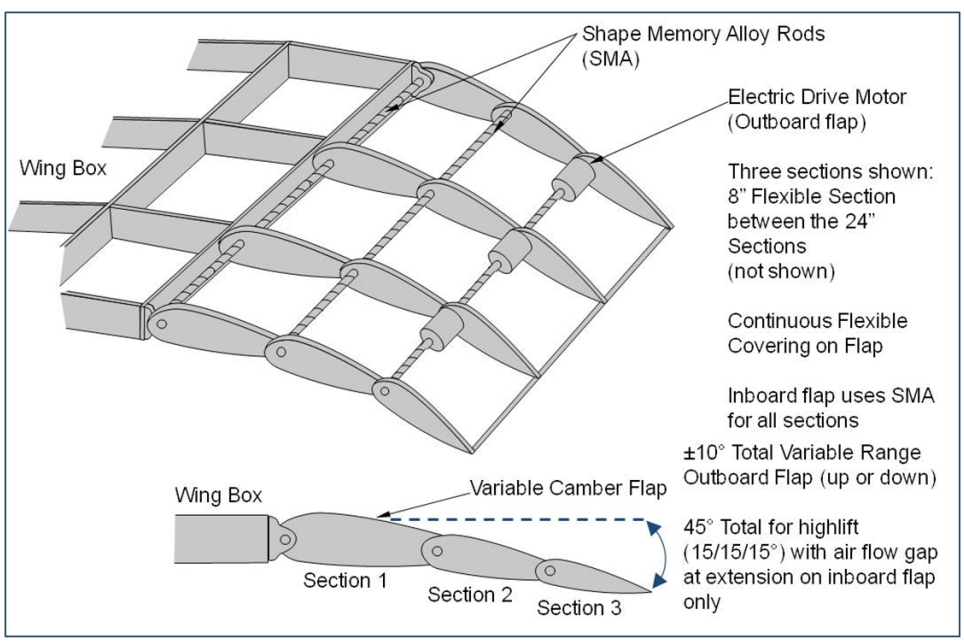

Figure 3. Variable Camber Flap Control Uses Shape Memory Alloy Torque Rod and Electric Drive Actuation

Figure 3 shows a schematic representation of an outboard wing flap section having three cambered flap segments.[4] SMA actuators drive the first and second cambered flap segments and a faster acting electric actuator drives the third cambered flap segment. SMA actuators can deliver large hinge moments, but generally move at a slow rate. The outboard wing flap uses the full-span third cambered segment as a roll command effector and as a control device for suppressing aeroelastic wing structural dynamic modes, both requiring high rates which can be met by electric

actuators.

Using the camber positioning, a full-span, high-lift configuration can be activated that has no drag producing gaps and a low flap noise signature. This is shown in Fig. 4. To further augment lift, a slotted flap configuration is formed by an air passage between the wing and the inner flap that serves to improve airflow over the flap and keep the flow attached. This air passage appears only when the flaps are extended in the high lift configuration.

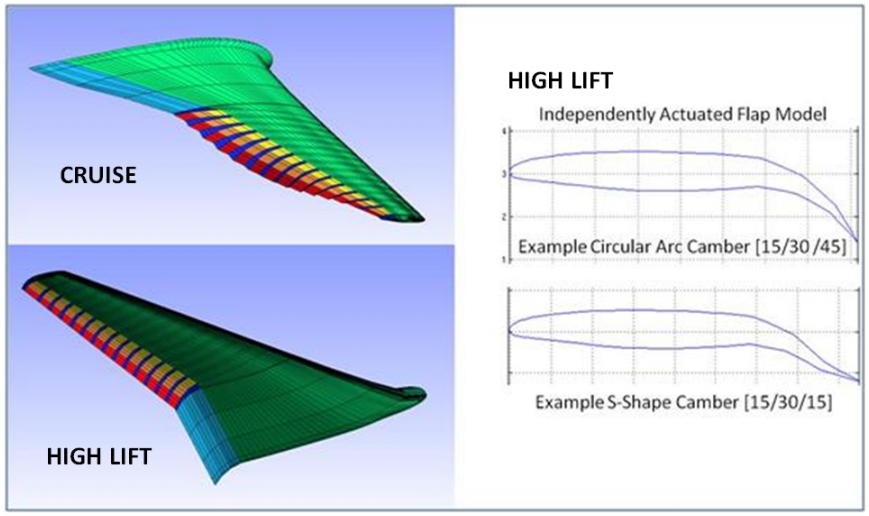

Figure 4. Cruise and High Lift VCCTEF Configurations

In the high-lift configuration, the outer wing flap uses the third cambered segment for roll control, as shown in Fig. 5. This provides rolling moment that is equivalent to aileron control. It is somewhat similar to deflecting the ailerons in a droop position to act as flaps, a common procedure used on tactical aircraft and on some transport aircraft.

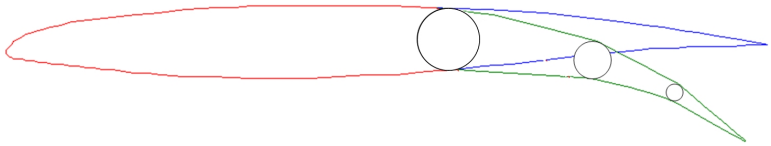

Figure 5. Three-Segment Variable Camber Flap

The high-lift configuration distributes the required flap hinge moment throughout the span of the wing while using actuation components that are all located interior to the wing and flap. This can be achieved by the use of SMA hinge line torque rods, sized to meet the hinge moment requirements at each spanwise location on the wing.

Figure 6 illustrates the GTM equipped with the VCCTEF for wing shaping control. By actively shaping the wing aerodynamic surface using the VCCTEF, optimal aerodynamic performance could potentially be realized at any point in the flight envelope. This is a mission-adaptive flexible wing concept. It is a key enabling feature of the research area Performance Adaptive Aeroelastic Wing (PAAW) in the AATT project. The term "performance adaptive aeroelastic" distinguishes itself from the earlier term "mission adaptive" in that the effect of aeroelasticity on aerodynamic performance must be fully accounted for as is the case for modern transport design. The VCCTEF relies on two mechanisms to improve aerodynamic performance: 1) wing twist optimization for flexible wing design, and 2) variable camber and continuous trailing edge for improved aerodynamics. This technology could enable modern high-aspect ratio flexible wing aircraft with significant flexibility to adaptively change wing shapes in-flight to achieve cruise drag optimization, while at the same time satisfying operational constraints such as structural load limitations, flutter margins, gust and maneuver load responses, and others by active aeroservoelastic controls.

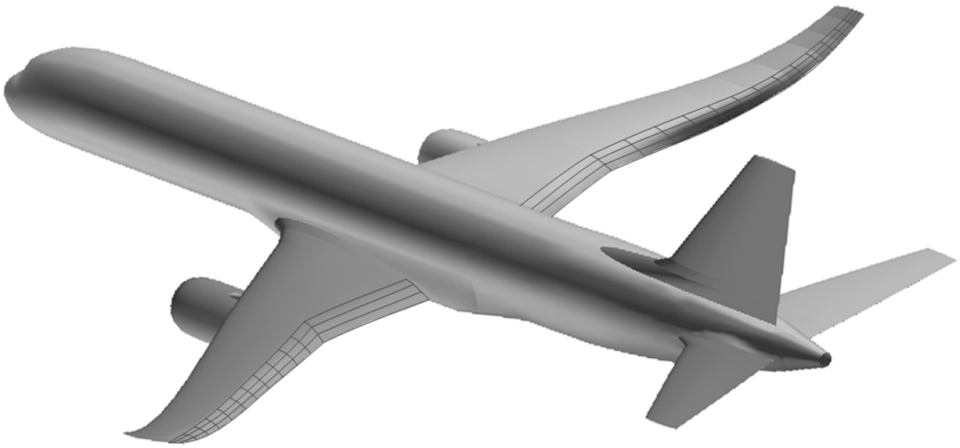

Figure 6. GTM with with Variable Camber Continuous Trailing Edge Flap

III. Wind Tunnel Model of Flexible Wing

For exploratory assessment of the aerodynamic potential of the VCCTEF concept, a 10%-scaled aeroelastic model of a softened Boeing 757-based GTM wing was constructed for a wind tunnel experimental investigation in the University of Washington Aeronautical Laboratory (UWAL). The semi-span of the model is 73.29 inches, as shown in Fig. 7. The wing model is constructed of woven fabric composites skin and extruded polystyrene foam core. The composite laminates and extruded polystyrene foam core are structurally tailored to attain half of the bending stiffness of the scaled baseline GTM wing while keeping torsional stiffness about the same. This tailored stiffness is to achieve a 10% wing tip deflection at 1-g conditions. The VCCTEF parts are fabricated by 3D printing. There are five spanwise VCCTEF sections, each with three cambered segments that form a trailing edge cambered surface. The flap segments are mechanically interlocking aerodynamic surfaces in the chordwise direction, as shown in Fig. 8. Plastic inserts are used to model a flexible transition material in between the spanwise flap sections. The flap segments are hinged at three chordwise locations and are designed to be fully adjustable. The dimensions of the VCCTEF are shown in Fig. 9. The center body of the wind tunnel model provides an aerodynamic fairing over the mounting of the wing to the wind tunnel's floor mount and was shortened somewhat relative to a full-scale airliner fuselage.

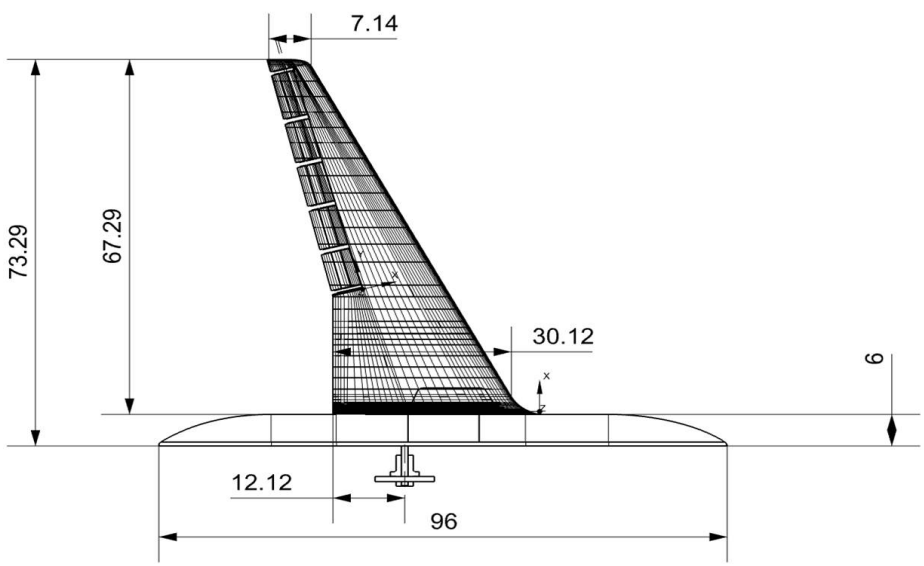

Figure 7. UWAL GTM Wing with VCCTEF in Cruise Configuration (Courtesy of University of Washington Aeronautical Laboratory)

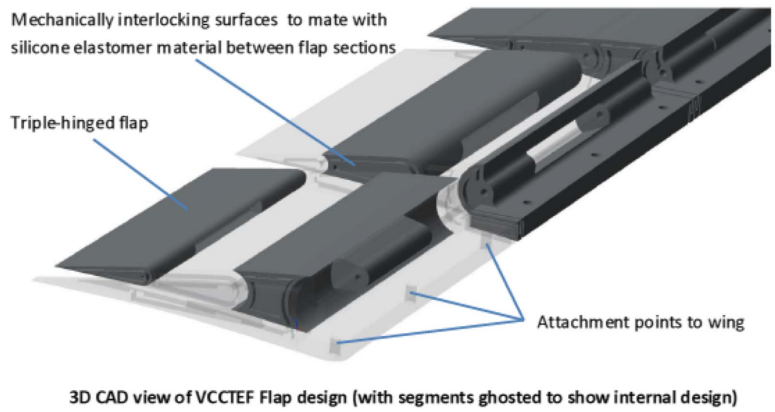

Figure 8. VCCTEF Construction (Courtesy of University of Washington Aeronautical Laboratory)

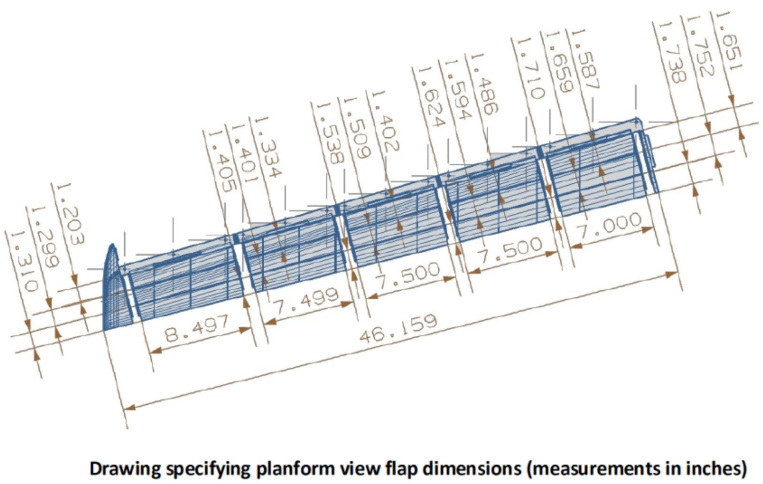

Figure 9. VCCTEF Dimension (Courtesy of University of Washington Aeronautical Laboratory)

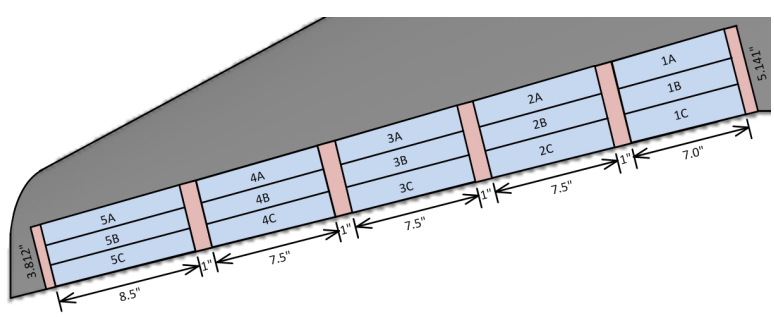

Figure 10. VCCTEF Flap Notation

The five VCCTEF flap sections are numbered from 1 at the inboard to 5 at the outboard. Each flap section is comprised of three cambered segments labeled as A for the innermost cambered segment, B for the middle cambered segment, and C for the trailing edge cambered segment. This is shown in Fig. 10. The position angle is denoted by $(a/b/c)$ where a, b, and c are flap positions in degrees relative to the forward flap segment. For segment A, the position angle is with respect to the fixed wing portion.

The relevant model scaling information is given in Table 1.

	Full-Scale	Semi-Span Model
M_∞	0.797	0.1162
C_L	0.51	0.51
h, ft	36,000	0
q_∞, psf	211.09	20.00
$S/2$, ft^2	975.5	9.638
$\bar{c}$, ft	16.6417	1.5963
$b/2$, ft	62.4167	6.1262

Table 1. Model Parameters

The wind tunnel test is designed to be an exploratory, proof-of-concept study. The objective of the wind tunnel experiment is to explore the relative merit of the VCCTEF design as a drag reduction control device, and the ability to simulate the problem in a relatively low-cost test. Lift, drag, side force, pitching moment, yawing moment, and rolling moment were recorded from the external floor-mounted balance. In addition, aeroelastic deflections of the flexible wing model were also measured by a VICON motion tracking system.[10] The VICON system measured a three-dimensional displacement field of the wind tunnel model at several target locations on the model.

IV. High-Lift Design and CFD Analysis

Typical high-lift flaps for transport aircraft use a Fowler flap design in conjunction with a leading edge device such as the Variable Camber Krueger (VCK) leading edge device to increase $C_{L_{max}}$. The Fowler motion requires flap track gearing mechanisms to translate the flap rearward to increase the effective wing surface area. These flap track mechanisms and the associated fairing covers can add a significant weight to the overall system weight. One option to simplify the high-lift system is to use the Fowler flap design only for the inboard high-lift flap. The outboard VCCTEF will not have the Fowler motion and instead will only rely on hinge-line actuation mechanisms provided by the SMA and electric actuators.

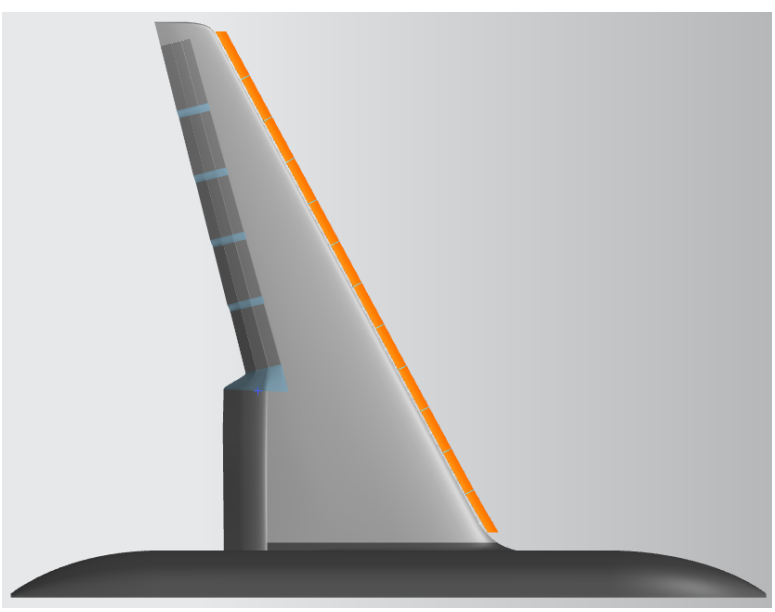

Figure 11. High-Lift Configuration of GTM Wing (Courtesy of University of Washington Aeronautical Laboratory)

Figure 11 illustrates the high-lift wind tunnel model.[11] Figure 12 is an assembly view showing the component build-up of the wind tunnel model. Because of the structural flexibility, the VCK leading edge device is fabricated in 12 individual segments with gap seals in between. The break in the VCK leading edge device is designed to allow the wing to bend without causing structural issues for the VCK and also to not introduce additional bending stiffness to the wing structure. Moreover, they are made to be individually adjustable. The VCK segments are attached to the

main wing structure by brackets as shown in Fig. 13. The VCK segments are numbered from 1 at the inboard to 12 at the outboard.

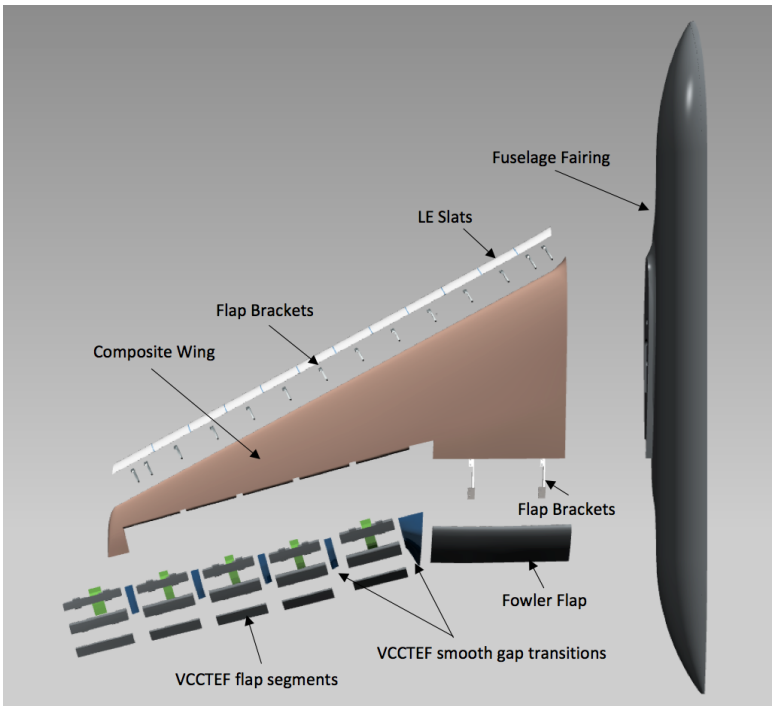

Figure 12. Exploded View of High-Lift GTM Wing (Courtesy of University of Washington Aeronautical Laboratory)

Figure 13. VCK Brackets (Courtesy of University of Washington Aeronautical Laboratory)

An OVERFLOW[12,13] 2D steady-state RANS CFD analysis was conducted to examine three different high-lift flap configurations: 1) a single-element plain flap at 30° deflection, 2) a three-segment cambered flap at $(20°/5°/5°)$ deflection, and 3) a three-segment cambered flap at $(10°/10°/10°)$ deflection. Two VCK rigging angles, 55° and 65°, were examined. The VCK rigging angles are relative to the forward projected airfoil centerline and not relative to a VCK under-wing stowed mechanical position. The Spalart-Allmaras turbulence model[14] is used with pre-specified laminar regions on the main wing element and flap, but the VCK is assumed to be in fully laminar flow. The flow

condition corresponds to the test section condition limited by balance load limit of 100 lbs at Mach 0.067 and Reynolds number 8.9×10^5.

The OVERFLOW 2D results show that the VCK rigged at 65° provides a much better attached flow at the wing leading edge than when it is rigged at 55°. This is shown in Fig. 14. The OVERFLOW results for the three different high-lift flap configurations indicate a significant flow separation associated with the cambered flaps as shown in Fig. 15. Thus, the baseline high-lift configuration was selected to be one with the VCK rigged at 65° and the single-element plain flap at 30° deflection. In addition, the cambered flap at $(10°/10°/10°)$ deflection was also fabricated and tested. It should be noted that the 2D lift prediction in general is more conservative than a 3D lift prediction due to the 3D spanwise relief. So the results only serve as a guide for the high-lift design.

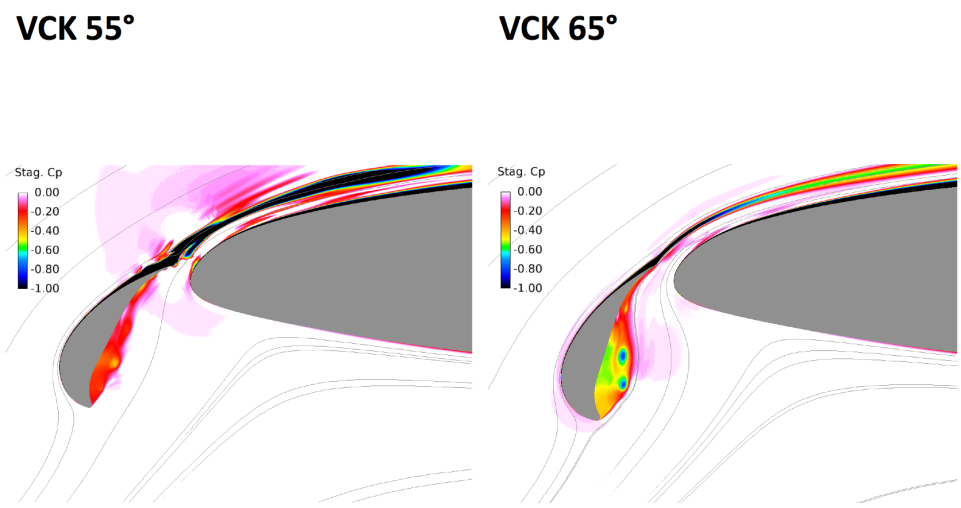

Figure 14. OVERFLOW 2D CFD Stagnation C_p Comparison for VCK Rigging Angles of 55° and 65°

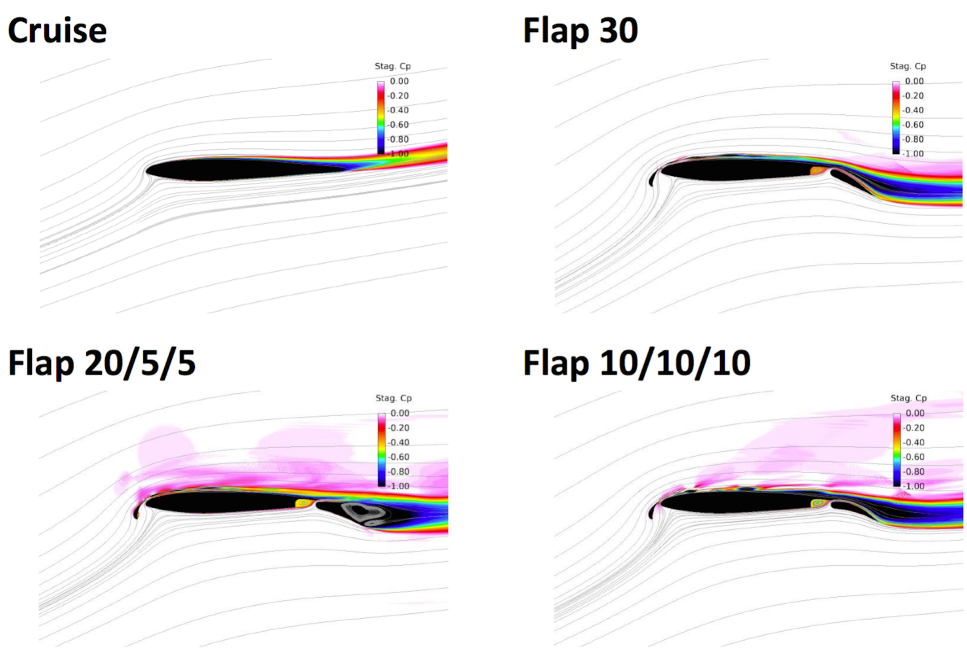

Figure 15. OVERFLOW 2D CFD Stagnation C_p Result at $\alpha = 14°$ with VCK Rigging Angle 65°

V. Wind Tunnel Test Results

Several configurations were tested in various combinations which include three wing configurations, three inboard high-lift flap configurations, five outboard VCCTEF configurations, six VCK configurations, and four Fowler slot configurations. These configurations are designated as

- W2.0 - Clean wing
- W2.1 - Wing with vortex generators (VG's) placed 1 inch aft of wing leading edge and spaced 6 inches between pairs.
- W2.2 - Wing with trip dots placed 0.5 inch back from wing leading edge.
- HLF0 - inboard high-lift plain flap with 0° deflection.
- HLF1 - inboard high-lift plain flap with 30° deflection.
- HLF2 - inboard high-lift three-segment cambered flap with $10^\circ/10^\circ/10^\circ$ deflection, where the individual flap deflections are defined relative to the forward wing or chordwise flap segment.
- VCK - Baseline VCK rigged at 65°.
- VCK1.1 - Baseline VCK with trip dots placed 1 inch from VCK leading edge.
- VCK1.2 - VCK with segments 8 to 12 rigged at a varying rigging angle from 65° to 60.5°.
- VCK1.3 - VCK with segments 8 to 12 rigged at 50°.
- VCK1.4 - VCK with segments 8 to 12 rigged at 50° and segments 5 to 7 rigged at 57.5°. In addition, the VCK slot width varies from segment 1 to 12 with values 0.350, 0.300, 0.350, 0.352, 0.251, 0.253, 0.205, 0.253, 0.254, 0.205, 0.200, and 0.253 inch.
- VCK1.5 - VCK1.1 configuration with VCK 3/8-inch trailing edge extension for outboard 10.75-inch of VCK.
- FLAP0 - VCCTEF deflections are set at $(0^\circ, 0^\circ, 0^\circ)$ for all flap sections.
- FLAP1 - VCCTEF deflections are set at $(10^\circ, 10^\circ, 10^\circ)$ for all flap sections.
- FLAP2 - VCCTEF deflections are set at $(10^\circ, 10^\circ, 10^\circ)$ for flap section 1, $(10^\circ, 10^\circ, 10^\circ)$ for flap section 2, $(10^\circ, 10^\circ, 10^\circ)$ for flap section 3, $(8^\circ, 8^\circ, 8^\circ)$ for flap section 4, and $(4^\circ, 4^\circ, 4^\circ)$ for flap section 5.
- FLAP3 - VCCTEF deflections are set at $(10^\circ, 10^\circ, 10^\circ)$ for flap section 1, $(8^\circ, 8^\circ, 8^\circ)$ for flap section 2, $(6^\circ, 6^\circ, 6^\circ)$ for flap section 3, $(4^\circ, 4^\circ, 4^\circ)$ for flap section 4, and $(2^\circ, 2^\circ, 2^\circ)$ for flap section 5.
- FLAP4 - VCCTEF deflections are set at $(10^\circ, 10^\circ, 10^\circ)$ for flap section 1, $(7^\circ, 7^\circ, 7^\circ)$ for flap section 2, $(4^\circ, 4^\circ, 4^\circ)$ for flap section 3, $(1^\circ, 1^\circ, 1^\circ)$ for flap section 4, and $(-2^\circ, -2^\circ, -2^\circ)$ for flap section 5.
- SLOT 0-4 - Fowler slot width 0 (SLOT0), 0.25 inch (SLOT1), 0.3 inch (SLOT2), 0.5 inch (SLOT3), and variable slot width from 0.3 inch at inboard to 0.1 inch at outboard of high lift flap (SLOT4).

There are a total of 58 test runs, of which the results from 44 runs were usable. The test run matrix is shown in Table 2.

Run Numbers	Configurations
3-9	B1
15-18	B1 + W2.0 + FLAP0
23, 24, 26	B1 + W2.0 + VCK + FLAP0
27	B1 + W2.1 + VCK + FLAP0
29, 30	B1 + W2.2 + VCK + HLF1 + FLAP4 + SLOT1
31-34, 36	B1 + W2.2 + VCK1.1 + HLF1 + FLAP4 + SLOT1
35	B1 + W2.2 + VCK1.5 + HLF1 + FLAP4 + SLOT1
37	B1 + W2.2 + VCK1.2 + HLF1 + FLAP4 + SLOT1
38	B1 + W2.2 + VCK1.3 + HLF1 + FLAP4 + SLOT1
39, 42	B1 + W2.2 + VCK1.4 + HLF1 + FLAP4 + SLOT1
40	B1 + W2.2 + VCK1.4 + HLF0 + FLAP0 + SLOT1
41	B1 + W2.2 + VCK1.4 + HLF1 + FLAP2 + SLOT1
43, 49, 50-55	B1 + W2.2 + VCK1.4 + HLF1 + FLAP1 + SLOT1
44	B1 + W2.2 + VCK1.4 + HLF1 + FLAP3 + SLOT1
45	B1 + W2.2 + VCK1.4 + HLF2 + FLAP4 + SLOT1
46	B1 + W2.2 + VCK1.4 + HLF1 + FLAP1 + SLOT4
47	B1 + W2.2 + VCK1.4 + HLF1 + FLAP1 + SLOT3
48	B1 + W2.2 + VCK1.4 + HLF1 + FLAP1 + SLOT2
56-58	B1 + W2.2 + VCK1.4 + HLF2 + FLAP1 + SLOT1

Table 2. UW2087 Test Run Matrix

The first ten runs were with the fuselage body alone. These runs are designated B1. Almost all of the high-lift test runs were conducted with the plain flap configuration HLF1. Runs 15 to 18 were designed to be repeat runs to compare with the clean wing data from the cruise configuration test in 2013. Runs 23 to 39 were exploratory runs to identify possible fixes to a premature stall of the baseline VCK configuration. Runs 40 to 58 are with the final configuration with the VCK re-rigged to the proper rigging angles, designated as VCK1.4.

Due to the balance load limit, the test was conducted at a nominal dynamic pressure of about 5.8 psf. Figure 16 is a photo of the high-lift wind tunnel model in the UWAL test section.

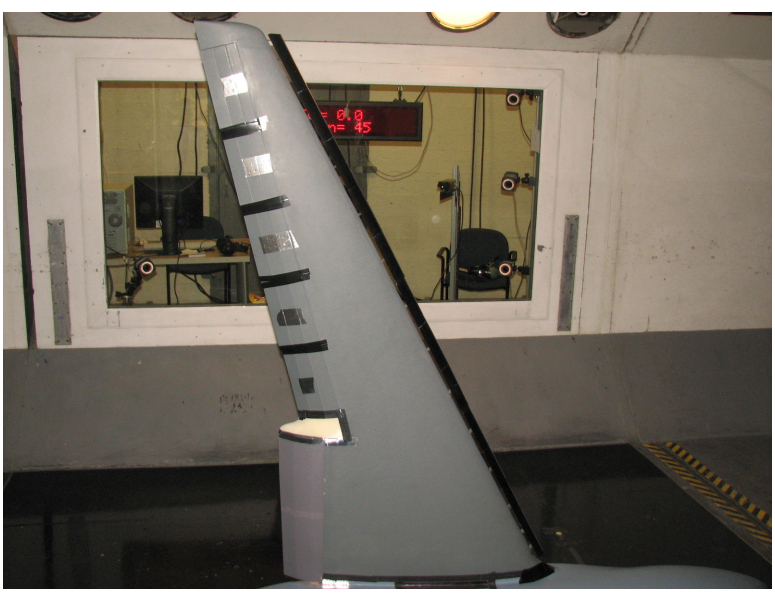

Figure 16. High-Lift Flexible Wing Wind Tunnel Model in UWAL Test Section (Courtesy of University of Washington Aeronautical Laboratory)

Figures 17(a) and (b) are the lift and drag curves versus the angle of attack for the clean wing repeat runs and one of the runs from the cruise configuration test in 2013 at about the same dynamic pressure.

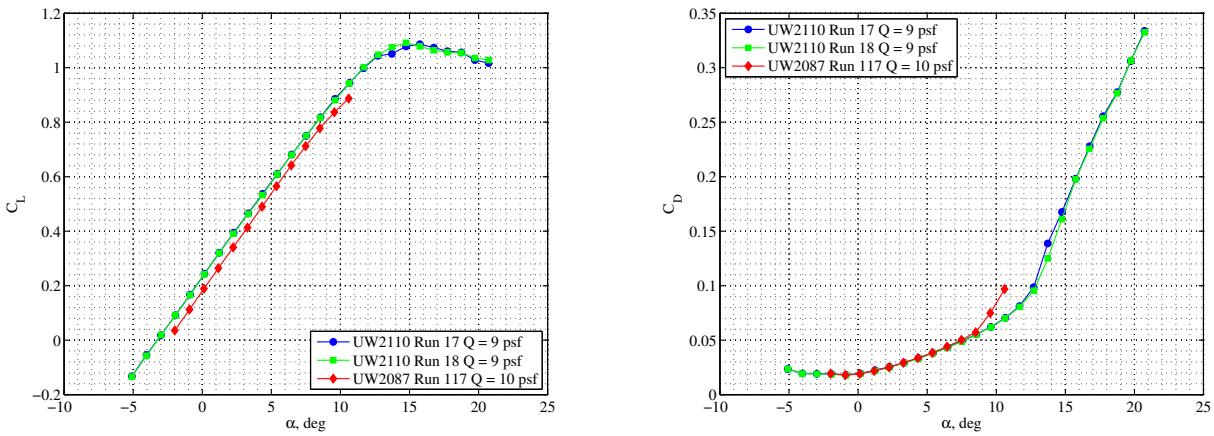

(a) (b)

Figure 17. Clean Wing C_L and C_D vs. α

The clean wing stalls at about $\alpha_{stall} = 15^\circ$ corresponding to $C_{L_{max}} = 1.09$ at $q_\infty = 9$ psf. The gradual stall characteristic is typical of a flow separation on the wing upper surface. The transition in the drag characteristic from parabolic to nearly linear with respect to the angle of attack is indicative of flow separation. Because the wind model is aeroelastically scaled so that the flexibility is representative of a full-scale transport wing, it actually exhibited low-frequency unsteady aeroelastic "bouncing" motion in the presence of stall buffet, very similar visually to full-scale transport wings during stall maneuvers.

Comparing to the clean wing run from the cruise configuration test, there is a marked shift in the lift curve. The clean wing in the cruise configuration test has a lower lift at the same angle than that in the high-lift test. The offset in the lift coefficient at zero angle of attack is $\Delta C_{L_0} = 0.05$ and the offset in the zero lift angle of attack is $\Delta\alpha_0 = -0.8^\circ$. The lift curve slopes between the two tests are about the same, thus indicating that the wing stiffness is nominally about the same as the stiffness affects mostly the lift curve slope. Thus, the bias in the two lift curves suggests a number of possibilities. One possibility is that the wing incidence angle between the two tests might be different. Another possibility is that the actual flap deflections were not at their correct settings during the cruise configuration test as observed in 2013.

It is also interesting to note that the last two points on the lift and drag curves from the cruise configuration test reveal a different characteristic in the data which could suggest a potential incipient stall behavior as the drag curve begins to break away from the nominal drag bucket at low angles of attack.

Some of the test data were reduced with fuselage force and moment contributions removed from the total force and moment measurements. These data are intended to provide wing-alone force and moment measurements. Figures 18(a) and (b) show the lift and drag comparison between the wing-fuselage and wing-alone measurements. By removing the fuselage contributions, lift and drag are reduced by a small amount, but more noticeably for drag. The difference in lift becomes more noticeable at higher angles of attack. The wing-alone data are deemed not as useful for a CFD validation or a correlation with a full-scale wing-body configuration. Therefore, all the test data subsequently reported in the paper include the total force and moment measurements on the wing-fuselage wind tunnel model.

Figures 19(a) and (b) are the plots of the lift and drag curves with the baseline VCK installed on the otherwise clean wing. The VCK is designed to extend the range of $C_{L_{max}}$ by increasing the effective wing surface area and the camber at the leading edge for low-speed flow. The powerful effect of the VCK on lift is noticed as the $C_{L_{max}}$ value increases from about 1.04 for clean wing at $q_\infty = 4$ psf to 1.57 at $q_\infty = 6$ psf. The lift curve at low angles of attack is generally nonlinear. The lift coefficient with the VCK is lower than that for the clean wing at the same angle of attack. A significant increase in drag also accompanies. The sharp break in the lift curve at $\alpha = 17^\circ$ is indicative of an abrupt stall due to a premature flow separation associated with the VCK. This abrupt stall was observed during the wind tunnel test as an audible source of high-frequency acoustic signal emitting from the model. Because of the abrupt stall, the potential to achieve the highest possible $C_{L_{max}}$ was limited by the baseline VCK.

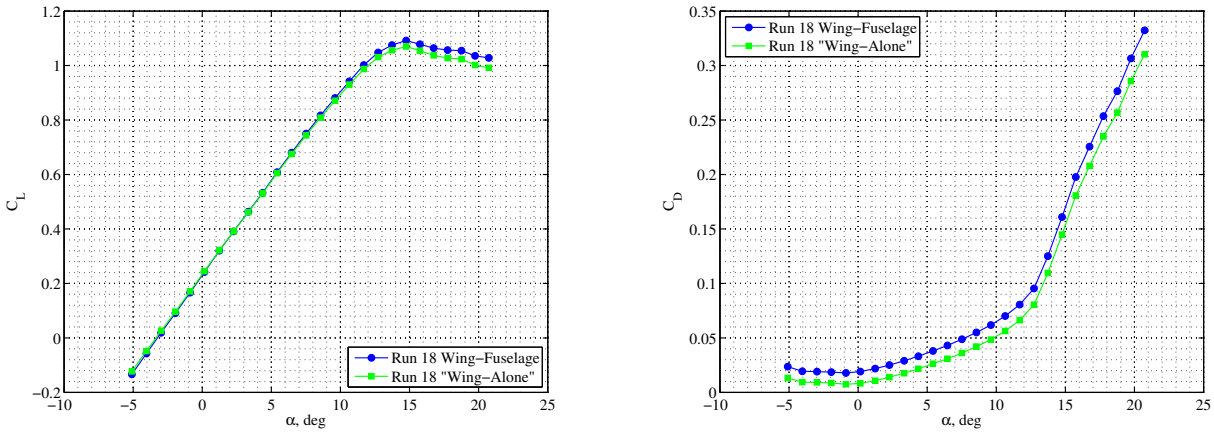

(a) (b)

Figure 18. Tare Correction on Clean Wing C_L and C_D vs. α

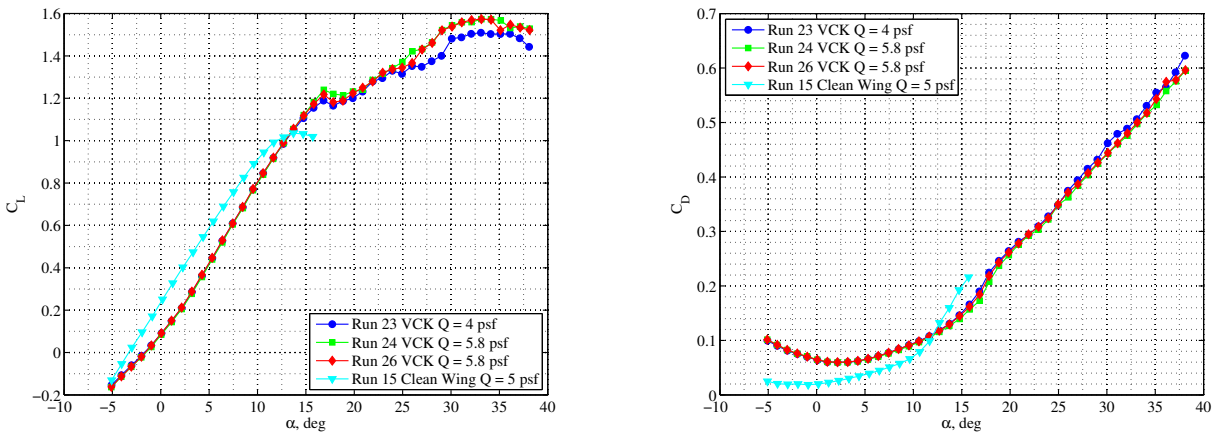

(a) (b)

Figure 19. Clean Wing with Baseline VCK C_L and C_D vs. α

Tufts were installed on the model for flow visualization which revealed aerodynamic issues with flow separation in the wing outboard area. This suggests that the 65° rigging angle was not optimal for the outboard VCK segments. The 2D CFD analysis was performed for the inboard wing section with the high-lift Fowler flap. Therefore the 65° rigging angle is only suitable for the inboard VCK segments.

Because of the noted abrupt stall of the baseline VCK, during the next several runs, various attempts were made to correct the premature flow separation of the VCK. Some simple solutions such as vortex generators (VG's) and boundary layer trip dots were attempted but did not seem to improve the flow. The most effective solution was to re-rig the VCK segments to different rigging angles. Five different VCK rigging configurations were tried. The VCK1.4 configuration was found to be the best among the five configurations. The re-rigging was accomplished by adding wedged shims to the VCK attachment brackets as shown in Fig. 20. In addition, because the high-lift test was conducted at fairly low Reynolds numbers where a significant portion of the wing could be in the laminar boundary layer, trip dots were placed on the main wing very close to the leading edge, shown in Fig. 21, in order to transition the flow to a fully turbulent flow over the main wing.

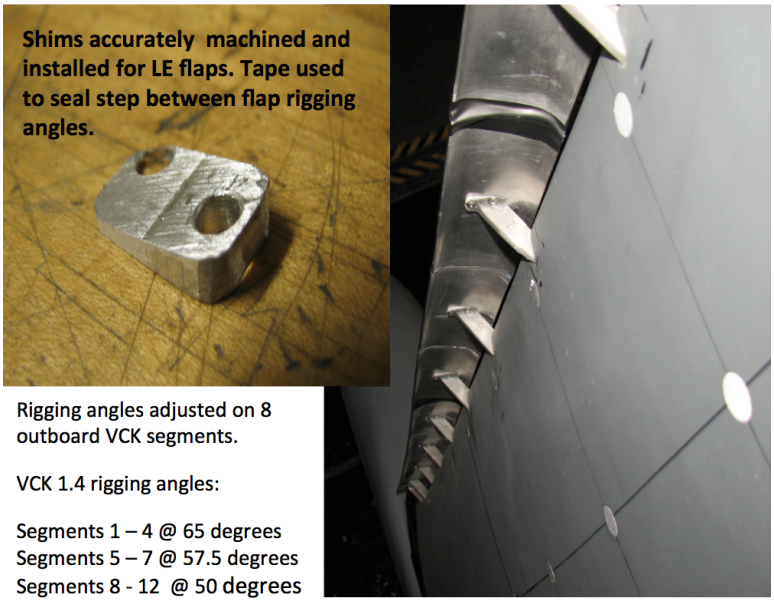

Figure 20. VCK Re-Rigging (Courtesy of University of Washington Aeronautical Laboratory)

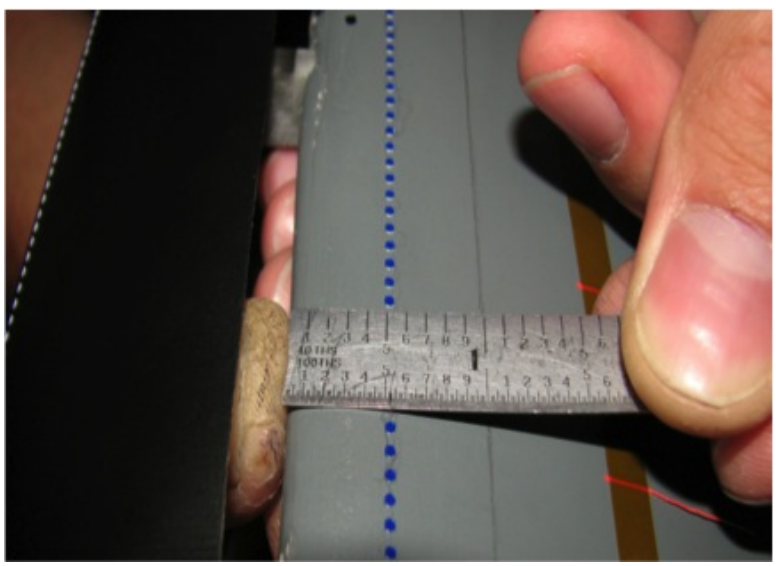

Figure 21. Boundary Layer Trip Dots on Main Wing (Courtesy of University of Washington Aeronautical Laboratory)

Figures 22(a) and (b) are the lift and drag curves for the baseline VCK with the VG's. Adding the VG's did not help improve the flow and actually worsens the stall characteristic.

Figures 23(a) and (b) are the lift and drag curves for all the five VCK re-rigging configurations with the high-lift plain flap configuration HLF1 and the VCCTEF configuration FLAP4. This represents a typical high-lift configuration for approach. It is apparent that the VCK1.4 configuration was able to extend the range of the angle of attack up to $\alpha_{stall} = 21.5^\circ$ corresponding to the highest $C_{L_{max}} = 2.09$. In contrast, the baseline VCK stalls at $\alpha_{stall} = 17^\circ$ corresponding to $C_{L_{max}} = 1.73$. All other VCK configurations more or less perform about the same. The VCK1.4 configuration also results in lower drag than the other VCK configurations since the flow is attached at higher angles of attack than the other configurations. The VCK1.4 configuration is then used for the rest of the test. It is noted that this $C_{L_{max}}$ value is close to the desired $C_{L_{max}}$ for a typical transport landing configuration. Thus, it appears that a viable level of high-lift performance could be attained with the VCK1.4 configuration.

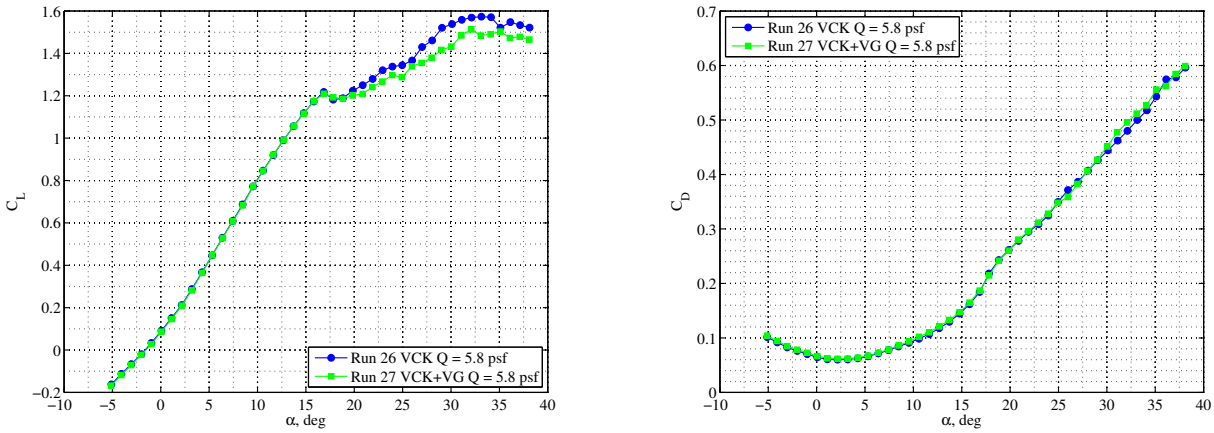

(a) (b)

Figure 22. Baseline VCK with Vortex Generators - C_L and C_D vs. α

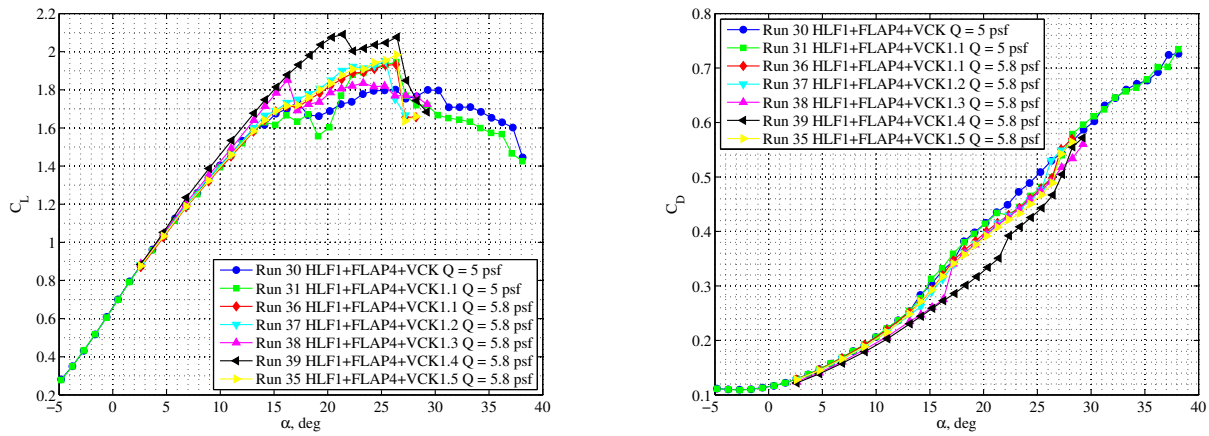

(a) (b)

Figure 23. VCK Comparison - C_L and C_D vs. α

Figures 24(a) and (b) are the comparison of the lift curves and drag polars for the clean wing, the high-lift plain flap configuration HLF1+FLAP4+VCK1.4, and the high-lift configuration HLF0+FLAP0+VCK1.4. An incremental maximum lift coefficient of $\Delta C_{L_{max}} = 1.05$ is achieved with the high-lift configuration HLF1+FLAP4+VCK1.4. The incremental lift coefficient between the high-lift configuration HLF1+FLAP4+VCK1.4 and HLF0+FLAP0+VCK1.4 is $\Delta C_L = 0.6$. The stall angle of attack at zero flap deflection occurs at $\alpha_{stall} = 24°$ which is about 2.5° higher than with the flap deflection. This is a typical stall characteristic of a wing-flap system.

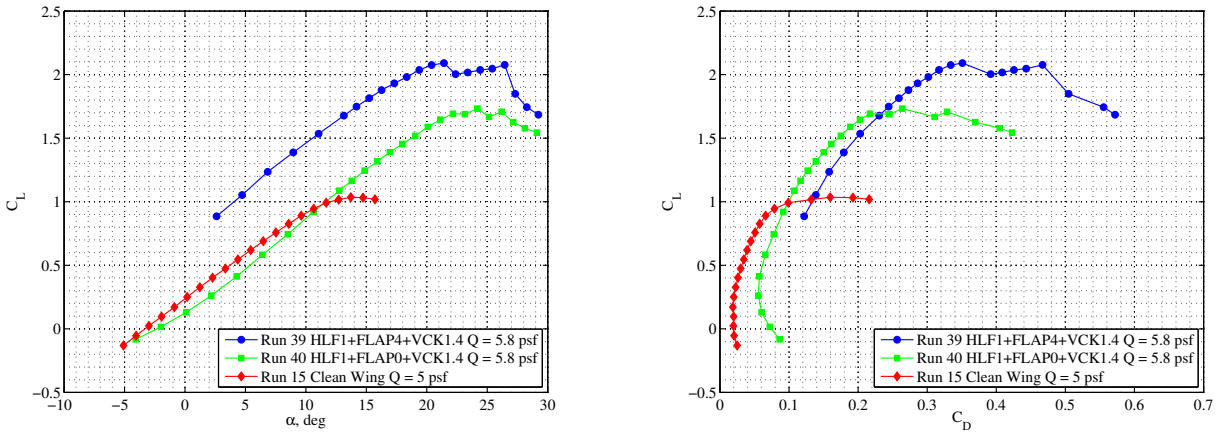

(a) (b)

Figure 24. High-Lift Plain Flap Comparison with Clean Wing - C_L vs. α and C_L vs. C_D

Figures 25(a) and (b) are the comparison of the lift and drag curves for different VCCTEF configurations FLAP1 through FLAP4 with the high-lift HLF1+VCK1.4 configuration. Both FLAP1 and FLAP2 configurations achieve about the same $C_{L_{max}} = 2.13$. Figures 26(a) and (b) are the drag polars and L/D curves for the high-lift configuration HLF1+VCK4. FLAP3 configuration has the highest L/D. The flap deflection for this configuration has a nearly elliptic distribution.

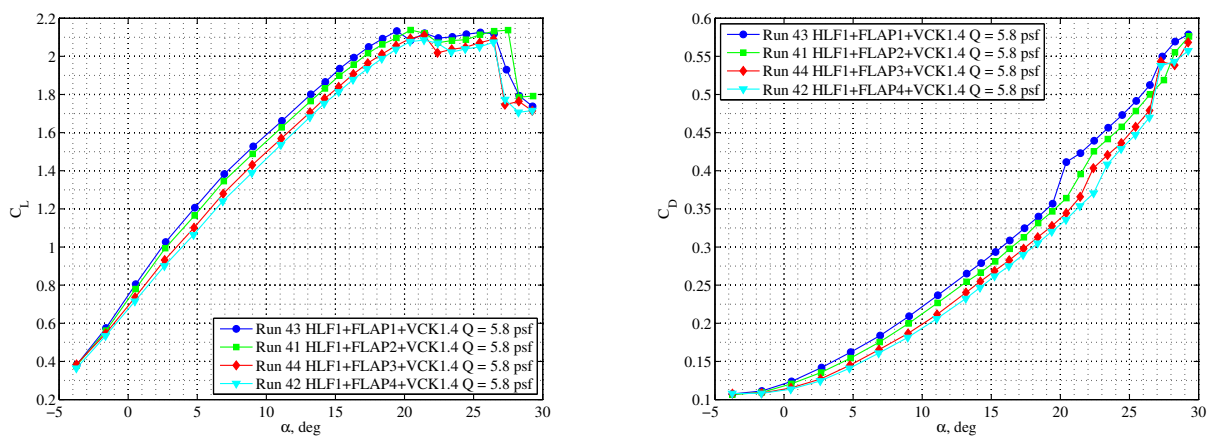

(a) (b)

Figure 25. High-Lift Plain Flap with Different VCCTEF Configurations - C_L and C_D vs. α

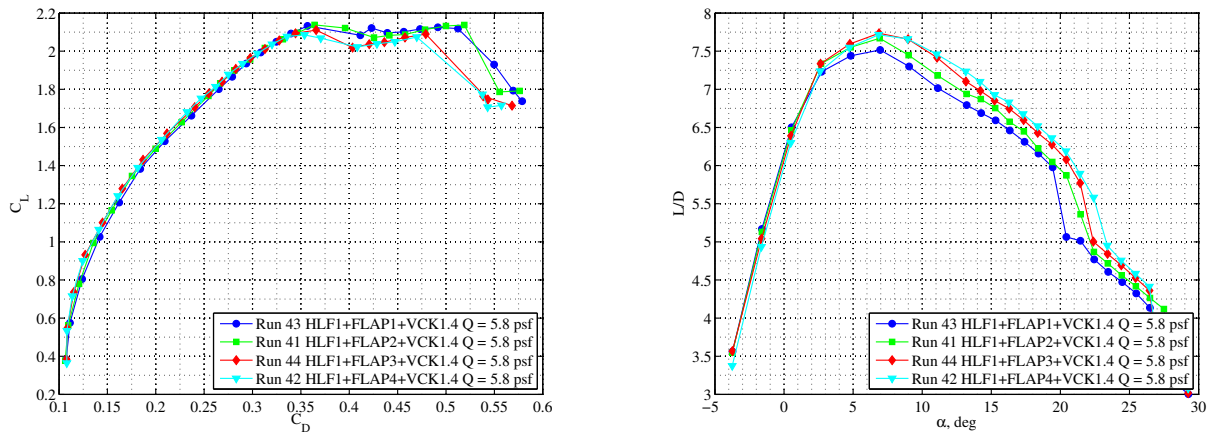

(a) (b)

Figure 26. High-Lift Plain Flap with Different VCCTEF Configurations - C_L **vs.** C_D **and** L/D **vs.** α

The high-lift plain flap is the baseline high-lift configuration, In addition, the high-lift cambered flap was also tested. For the same deflection, a cambered flap produces less lift and lower drag than a plain flap. This reduction in lift is consistent with aerodynamic theory. The lift coefficient for a cambered flap can be estimated using the potential flow theory. By deploying a flap, the effective angle of attack of a wing section increases. This effective angle of attack results in an incremental lift which can be estimated from 2D thin airfoil potential flow theory by the following formula:[7]

$$\Delta c_L = c_{L_\alpha} \sum_{i=1}^{N} \frac{\partial \alpha}{\partial \delta_i} \delta_i \tag{1}$$

where $\frac{\partial \alpha}{\partial \delta_i}$ is the angle of attack sensitivity which is given by

$$\frac{\partial \alpha}{\partial \delta_i} = \left. \frac{\cos^{-1}(-c^*) - \sqrt{1-c^{*2}}}{\pi} \right|_{c_i^*}^{c_{i+1}^*} \tag{2}$$

where $c^* = 1 - 2\frac{x_i}{c}$, c is the airfoil chord, and x_i is the flap hinge position of the i-th flap segment measured normal to the hinge axis from the leading edge.

The drag reduction comes from the profile drag which is lower for a cambered flap than a plain flap for the same trailing edge deflection angle or the same lift coefficient. Figures 27(a) and (b) are the comparison of the lift and drag curves between the plain flap configuration HLF1 and the cambered flap configuration HLF2, both deflected to a 30° deflection angle at the trailing edge. The cambered flap, as expected, produces less lift with $C_{L_{max}} = 2.04$ versus $C_{L_{max}} = 2.09$ for the plain flap, a 2.4% reduction. On the other hand, the drag coefficient of the cambered flap is about 0.02 (200 drag counts) less than the drag coefficient of the plain flap up to the stall angle of attack as shown in Fig. 27(b). This drag offset is due to the reduced profile drag on the cambered flap. Figures 28(a) and (b) are the drag polar and the L/D plots of the cambered flap and plain flap. The cambered flap produces about 6% improvement in L/D over the plain flap, which translates into a 6% reduction in the profile drag at the maximum L/D. While at high-lift conditions, lift production is the most important requirement, the results confirm the drag reduction benefit of the three-segment cambered flap which could favorably impact engine-out climb gradients and community noise.

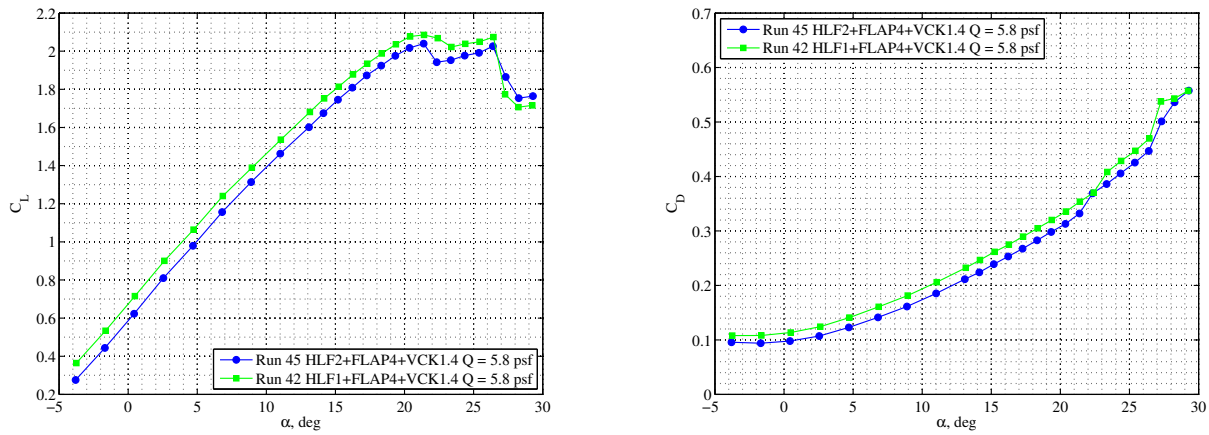

(a) (b)

Figure 27. High-Lift Plain Flap vs. Cambered Flap - C_L vs. α and C_L vs. C_D

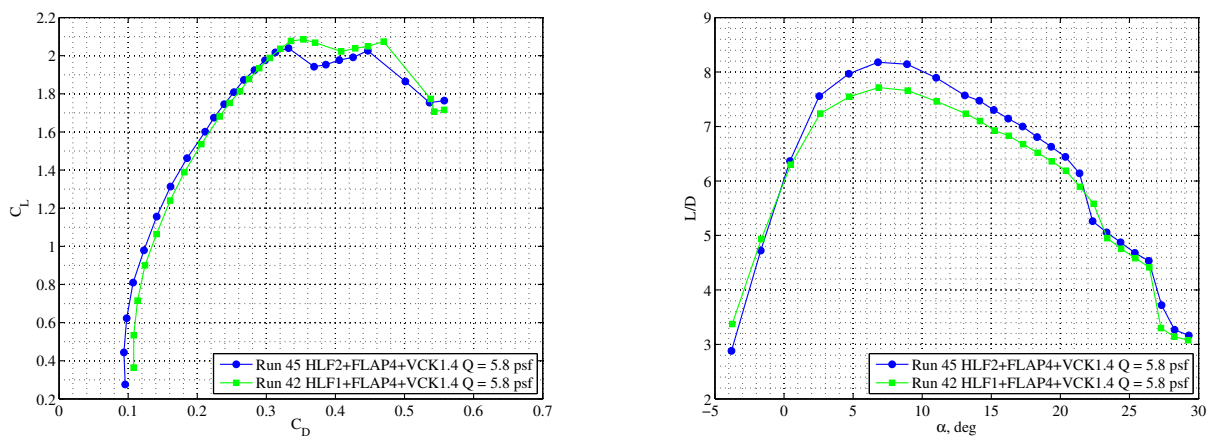

(a) (b)

Figure 28. High-Lift Plain Flap vs. Cambered Flap - C_L vs. C_D and L/D vs. α

The effect of the Fowler slot width was investigated with three additional slot width configurations over the baseline slot width of 0.25 inch. Figure 29(a) shows the lift curves for the high-lift configuration HLF1+FLAP4+VCK1.4 with different Fowler slot widths. The varying slot width SLOT4 configuration produces the lowest value of $C_{L_{max}}$. As the slot width increases, an increase in the effective wing area results, but at the same time, the flow through the wider slot transports less kinetic energy to re-energize the boundary layer to maintain attached flow. A correlation of $C_{L_{max}}$ with the Fowler slot width is established based on the following formula:

$$\frac{C_{L_{max}}}{C_{L_{max,ref}}} = a - be^{-c\frac{w}{\bar{c}}} \tag{3}$$

where w is the slot width and $\bar{c}$ is the mean aerodynamic chord.

The reference slot width is $w_{ref} = 0.25$ inch. Figure 29(b) shows the correlation of $C_{L_{max}}$ with the slot width-to-mean aerodynamic chord ratio $w/\bar{c}$. The correlation results in $a = 1.00637$, $b = 0.219788$, and $c = 0.739725$.

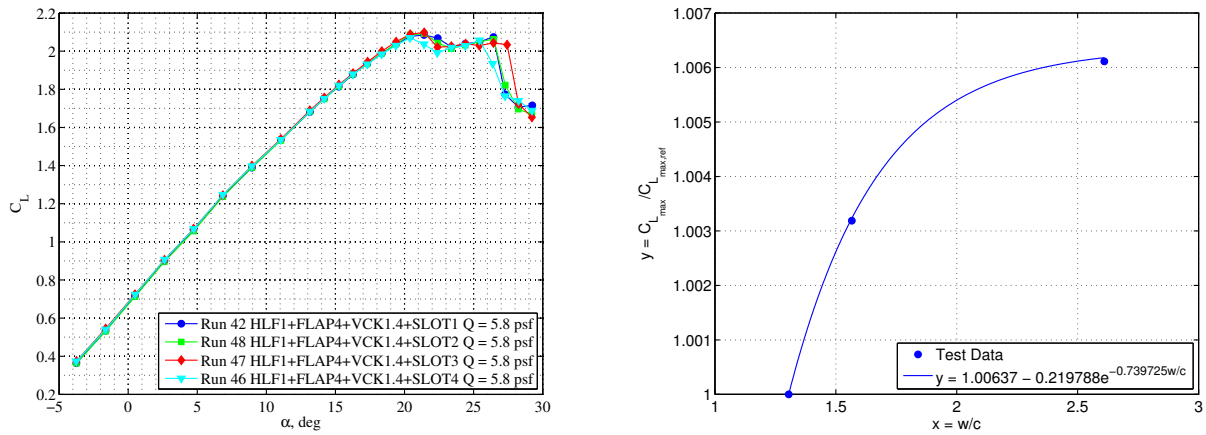

(a) (b)

Figure 29. Effect of Fowler Slot Width - C_L vs. α and $C_{L_{max}}$ vs. Width w

The Reynolds number / aeroelastic effect was also investigated for both the plain flap and cambered flap configurations HLF1 and HLF2. It should be noted that, because the flexible wing wind tunnel model is an aeroelastic model with a significant wing aeroelastic deflection, there is no "pure" Reynolds number effect. As the dynamic pressure changes, both the Reynolds number effect and aeroelastic effect act together to change lift. In general, $C_{L_{max}}$ increases with increasing the Reynolds number[15,16] but decreases with increasing the dynamic pressure for a sweptback wing.[7] Figures 30(a) and (b) are the lift curves and drag polars for the high-lift plain flap configuration HLF1+FLAP1+VCK1.4 at a varying dynamic pressure $q_\infty = 1$ psf to 5.8 psf. As the dynamic pressure, hence Reynolds number, increases, the skin friction coefficient decreases for a fully turbulent boundary layer.[17] As a result, viscous drag generally decreases while lift increases with increasing Reynolds number. This is evident in Figs. 30(a) and (b). This also suggests that the Reynolds number effect outweighs the aeroelastic effect at stall. Otherwise, the trend of increasing $C_{L_{max}}$ with increasing the dynamic pressure would have been reversed. There is a marked change in the lift and drag characteristics at $\alpha = 11^\circ$ for $q_\infty = 1$ psf, corresponding to a Reynolds number per unit length of 0.17906×10^6/ft, possibly indicating of a flow separation. At a dynamic pressure above 1 psf, the lift and drag characteristics appear similar.

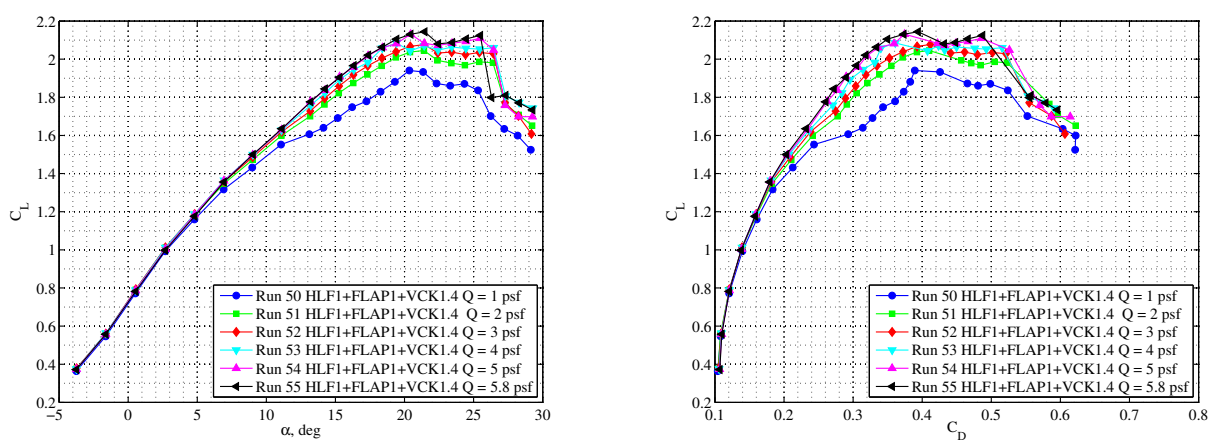

(a) (b)

Figure 30. Reynolds Number / Aeroelastic Effect for Plain Flap - C_L vs. α and C_L vs. C_D

Figure 31 (a) is a correlation of $C_{L_{max}}$ with the Reynolds number based on the suggested formula in Reference[15, 16]

$$\frac{C_{L_{max}}}{C_{L_{max,ref}}} = \left(\frac{Re}{Re_{ref}}\right)^a \tag{4}$$

where Re is the Reynolds number based on the mean aerodynamic chord, and a is obtained from curve-fitting.

The correlations with $C_{L_{max}}$ at $q_\infty = 1$ and 4 psf are not as good as with the other values of $C_{L_{max}}$. Using only the data for $q_\infty = 2$, 3, 5, and 5.8 psf, $a = 0.0896624$. Reference[16] suggests $a = 0.1$, which is in good agreement with the data.

For a typical transport aircraft similar the Boeing 757, a typical approach speed is about 140 knots at sea level. Using a conservative 30% stall speed margin, the stall speed is about 108 knots. This correspond to a flight Reynolds number of 19.2048×10^6 based on the MAC of 16.6417 ft. The reference Reynolds number for $q_\infty = 2$ psf is 0.402416×10^6. Thus, if the correlation equation (4) is used for the Reynolds number correction, a 40% increase in $C_{L_{max}}$ would result. It is obvious that the Reynolds number correction using low Reynolds number data based on the correlation equation (4) is not reliable. Also the correlation equation (4) may be applicable for a "pure" Reynolds number correction, but for an aeroelastic model, this correction may result in an over-estimation of $C_{L_{max}}$ since the aeroelastic effect causes $C_{L_{max}}$ to decrease with increasing the dynamic pressure.

An alternative correlation is sought based on an exponential function as

$$\frac{C_{L_{max}}}{C_{L_{max,ref}}} = a - be^{-c\left(\frac{Re}{Re_{ref}}\right)} \tag{5}$$

Discarding the data at $q_\infty = 4$ psf, the correlation yields $a = 1.13063$, $b = 0.409968$, and $c = 1.14775$, as shown in Fig. 31 (b). Applying this correlation to the flight Reynolds number results in 13% increase in $C_{L_{max}}$ over the baseline $C_{L_{max}} = 1.9409$ at 1 psf, or $C_{L_{max}} = 2.1944$, which seems to be reasonable.

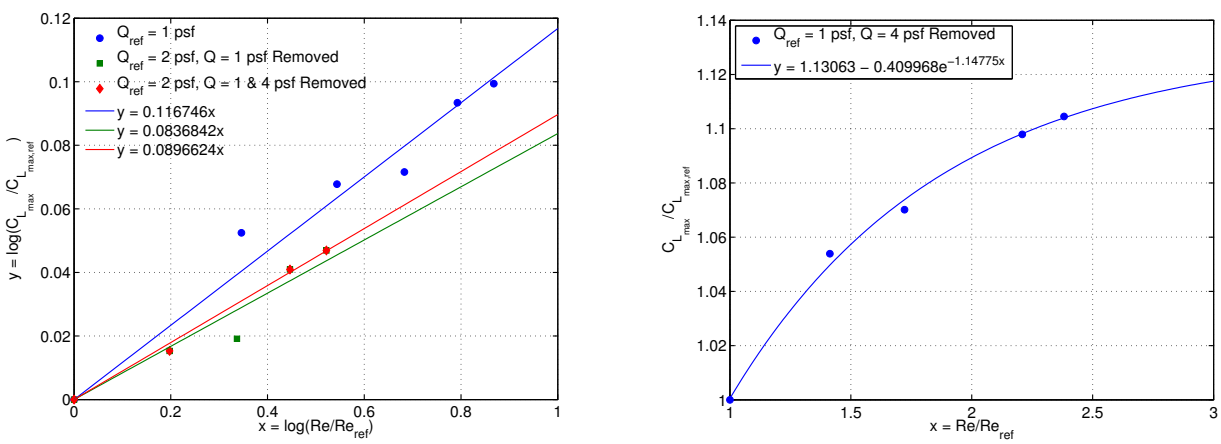

(a) (b)

Figure 31. $C_{L_{max}}$ **Correlations with Reynolds Number**

To correct for the Mach number effect, one can use the Prandtl-Glauert subsonic compressibility correction. This is only an approximate method since the flow at stall is nonlinear whereas the Prandtl-Glauert subsonic compressibility correction is applicable to linear subsonic flow. The Mach number correction factor also includes the effect of wing sweep. Thus

$$\frac{C_{L_{max}}}{C_{L_{max,ref}}} = \sqrt{\frac{1 - M_{\infty,ref}^2 \cos^2\Lambda}{1 - M_\infty^2 \cos^2\Lambda}} \tag{6}$$

where Λ is the sweep angle of the wing leading edge.

The stall speed is about Mach 0.16 whereas the reference speed is about Mach 0.03. For a sweep angle $\Lambda = 28°$, the Mach number correction results in 1% increase in $C_{L_{max}}$ or $C_{L_{max}} = 2.2169$.

It should be noted that the $C_{L_{max}}$ correlation is for a wing with no engine nacelle and no horizontal tail. So, the $C_{L_{max}}$estimate may not directly translate into a $C_{L_{max}}$ for a complete aircraft configuration. Nonetheless, this $C_{L_{max}}$

correlation can serve as a guide in the design of a high-lift system for a flexible wing transport similar to the high-lift configuration tested. Figures 32(a) and (b) illustrate the Reynolds number / aeroelastic effect on drag. As the dynamic pressure increases, drag decreases for $\alpha \gtrsim 0$ but actually increases for $\alpha \lesssim 0$ as seen in Fig. 32(a).

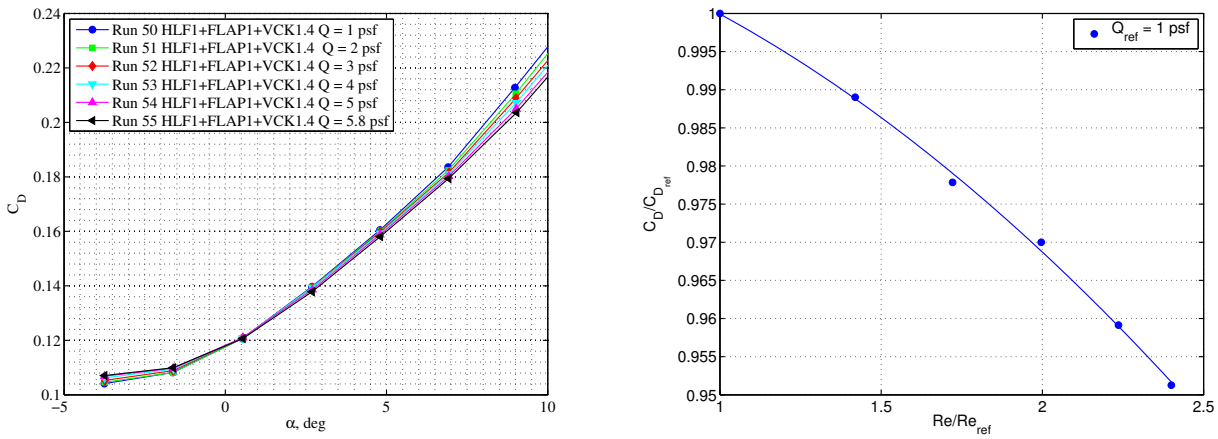

(a) (b)

Figure 32. Reynolds Number / Aeroelastic Effect - C_D vs. α and C_D Correlations with Reynolds Number at $\alpha = 10°$

Figures 33(a) and (b) are the lift curves and drag polars for the high-lift cambered flap configuration HLF2+FLAP1+VCK1.4 at $q_\infty = 1$, 2, and 5.8 psf. A similar Reynolds number effect is exhibited for the high-lift cambered flap. A $C_{L_{max}} = 2.09$ is achieved at a stall angle of attack $\alpha_{stall} = 20.4°$. The lift curve at $q_\infty = 5.8$ psf exhibits an abrupt stall which suggests that VCK1.4 configuration may need to be re-rigged. Since the cambered flap has a larger camber than the plain flap, the VCK rigging angle probably needs to be reduced to keep the effective camber about the same.

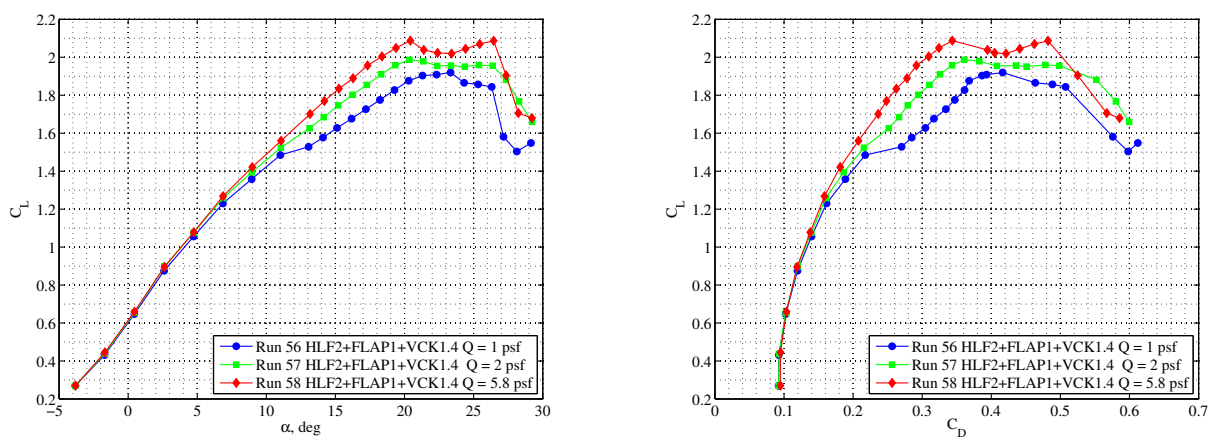

(a) (b)

Figure 33. Reynolds Number / Aeroelastic Effect for Cambered Flap - C_L vs. α and C_L vs. C_D

Figures 34(a) and (b) shows the correlation of $C_{L_{max}}$ with the Reynolds number based on Eq. (5) and the Reynolds number effect on C_D at $\alpha = 10°$. The lift correlation yields the parameters $a = 1.13063$, $b = 0.292805$, and $c = 0.804576$. The Reynolds number correction results in a 13% increase in $C_{L_{max}}$ at the flight Reynolds number, or an estimate of $C_{L_{max}} = 2.1705$. Applying the Prandtl-Glauert mach number correction results in an estimated $C_{L_{max}} = 2.1927$.

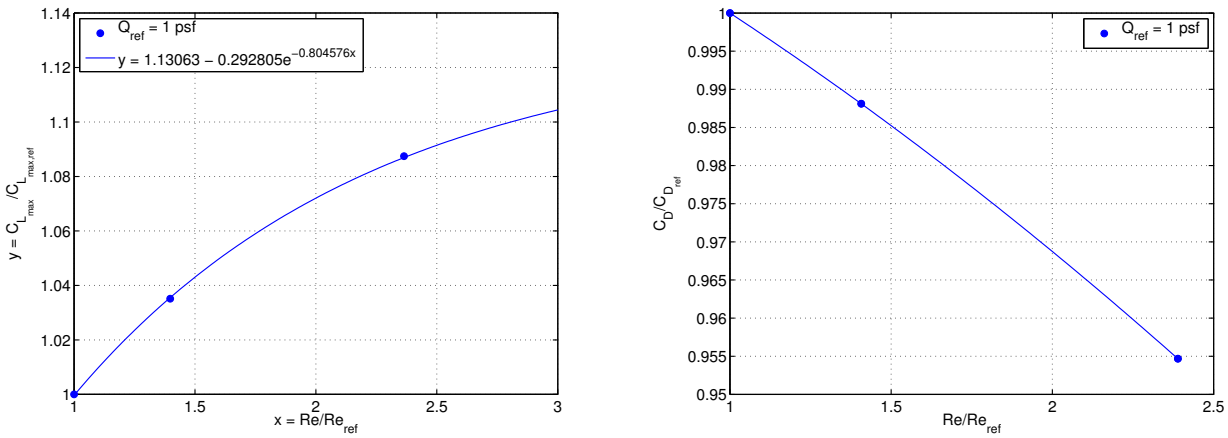

(a) (b)

Figure 34. $C_{L_{max}}$ **vs.** Re **and** C_D **vs.** Re **at** $\alpha = 10^\circ$ **for Cambered Flap**

VI. Aeroelastic Analysis

Aeroelasticity affects the lift distribution of a flexible wing. For linear aerodynamics, the lift coefficient of a flexible wing section is computed as

$$C_L = \frac{1}{S}\int_{-b/2}^{b/2} c_{L\alpha}^{*}\left(\alpha_r + \alpha_e\right) dy \tag{7}$$

where $c_{L\alpha}^{*}\left(\bar{y}\right)$ is the rigid section lift curve slope, $\alpha_r\left(y\right)$ is the rigid local angle of attack, and $\alpha_e\left(y\right)$ is the elastic angle of attack which is given by[18]

$$\alpha_e\left(y\right) = \Theta\left(\bar{y}\right)\cos\Lambda - \frac{\partial W\left(\bar{y}\right)}{\partial \bar{y}}\sin\Lambda \tag{8}$$

where Θ is the wing torsional twist about the elastic axis $\bar{y}$ (positive leading edge up), W is wing bending deflection along the elastic axis (positive upward), and Λ is the sweep angle of the elastic axis.

The wing bending deflection and torsional twist are described by the coupled bending-torsion aeroelastic equations

$$\begin{aligned}\frac{\partial^2}{\partial \bar{y}^2}\left(EI_{yy}\frac{\partial^2 W}{\partial \bar{y}^2}\right) &= c_{L\alpha}^{*} q_\infty c\cos\Lambda\left(\alpha_r + \Theta\cos\Lambda - \frac{\partial W}{\partial \bar{y}}\sin\Lambda\right)\\ &\quad + \frac{\partial}{\partial x}\left[c_{m_{ac}} q_\infty c^2 + c_{L\alpha}^{*} q_\infty c e\left(\alpha_r + \Theta\cos\Lambda - \frac{\partial W}{\partial \bar{y}}\sin\Lambda\right)\right]\cos\Lambda\sin\Lambda\end{aligned} \tag{9}$$

$$-\frac{\partial}{\partial \bar{y}}\left(GJ\frac{\partial \Theta}{\partial \bar{y}}\right) = \left[c_{m_{ac}} q_\infty c^2 + c_{L\alpha}^{*} q_\infty c e\left(\alpha_r + \Theta\cos\Lambda - \frac{\partial W}{\partial \bar{y}}\sin\Lambda\right)\right]\cos^2\Lambda \tag{10}$$

where e is the offset of the elastic center from the aerodynamic center in the streamwise direction.

The weak-form expression of the aeroelastic equations can be formulated as

$$\left(\mathbf{K} + q_\infty\frac{\mathbf{K}_a}{q_\infty}\right)\mathbf{U} = q_\infty\left(\frac{\mathbf{F}_\alpha}{q_\infty}\alpha + \frac{\mathbf{F}_0}{q_\infty}\right) = q_\infty\frac{\mathbf{F}}{q_\infty} \tag{11}$$

where $\mathbf{K}$ is the generalized structural stiffness, $\mathbf{K}_a$ is the generalized aerodynamic stiffness, $\mathbf{U} = \begin{bmatrix}\mathbf{W}^\top & \Theta^\top\end{bmatrix}^\top$ is the generalized displacement vector, $\mathbf{F}_\alpha$ is the generalized aerodynamic force derivative with respect to the angle of attack, and $\mathbf{F}_0$ is the generalized aerodynamic force at zero angle of attack.

The generalized displacement is then expressed as

$$\mathbf{U} = \left(\mathbf{K} + q_\infty\frac{\mathbf{K}_a}{q_\infty}\right)^{-1}\left(\mathbf{F}_\alpha\alpha + \mathbf{F}_0\right) \tag{12}$$

Thus, the wing bending and torsional twist are function of the angle of attack as

$$W(\bar{y}) = \sum_{i=1}^{N} \Phi_i(\bar{y}) W_i = \Phi(\bar{y}) \mathbf{W} = W_\alpha(\bar{y}) \alpha + W_0(\bar{y}) \tag{13}$$

$$\Theta(\bar{y}) = \sum_{i=1}^{N} \Psi_i(\bar{y}) \Theta_i = \Psi(\bar{y}) \Theta = \Theta_\alpha(\bar{y}) \alpha + \Theta_0(\bar{y}) \tag{14}$$

where $\Phi(\bar{y})$ and $\Psi(\bar{y})$ are the bending and torsional mode shapes, and

$$W_\alpha(\bar{y}) = \begin{bmatrix} \Phi(\bar{y}) & \mathbf{0} \end{bmatrix} \left(\mathbf{K} + q_\infty \frac{\mathbf{K}_a}{q_\infty} \right)^{-1} q_\infty \frac{\mathbf{F}_\alpha}{q_\infty} \tag{15}$$

$$W_0(\bar{y}) = \begin{bmatrix} \Phi(\bar{y}) & \mathbf{0} \end{bmatrix} \left(\mathbf{K} + q_\infty \frac{\mathbf{K}_a}{q_\infty} \right)^{-1} q_\infty \frac{\mathbf{F}_0}{q_\infty} \tag{16}$$

$$\Theta_\alpha(\bar{y}) = \begin{bmatrix} \mathbf{0} & \Psi(\bar{y}) \end{bmatrix} \left(\mathbf{K} + q_\infty \frac{\mathbf{K}_a}{q_\infty} \right)^{-1} q_\infty \frac{\mathbf{F}_\alpha}{q_\infty} \tag{17}$$

$$\Theta_0(\bar{y}) = \begin{bmatrix} \mathbf{0} & \Psi(\bar{y}) \end{bmatrix} \left(\mathbf{K} + q_\infty \frac{\mathbf{K}_a}{q_\infty} \right)^{-1} q_\infty \frac{\mathbf{F}_0}{q_\infty} \tag{18}$$

For small q_∞, the inverse of the total stiffness matrix is approximated by a series expansion as

$$\left(\mathbf{K} + q_\infty \frac{\mathbf{K}_a}{q_\infty} \right)^{-1} \approx \mathbf{K}^{-1} - q_\infty \mathbf{K}^{-1} \frac{\mathbf{K}_a}{q_\infty} \mathbf{K}^{-1} + q_\infty^2 \mathbf{K}^{-1} \frac{\mathbf{K}_a}{q_\infty} \mathbf{K}^{-1} \frac{\mathbf{K}_a}{q_\infty} \mathbf{K}^{-1} \tag{19}$$

Then, $W(\bar{y})$ and $\Theta(\bar{y})$ vary approximately as cubic functions of the dynamic pressure as

$$W(\bar{y}) \approx \begin{bmatrix} \Phi(\bar{y}) & \mathbf{0} \end{bmatrix} \left(q_\infty \mathbf{K}^{-1} - q_\infty^2 \mathbf{K}^{-1} \frac{\mathbf{K}_a}{q_\infty} \mathbf{K}^{-1} + q_\infty^3 \mathbf{K}^{-1} \frac{\mathbf{K}_a}{q_\infty} \mathbf{K}^{-1} \frac{\mathbf{K}_a}{q_\infty} \mathbf{K}^{-1} \right) \left(\frac{\mathbf{F}_\alpha}{q_\infty} \alpha + \frac{\mathbf{F}_0}{q_\infty} \right) \tag{20}$$

$$\Theta(\bar{y}) \approx \begin{bmatrix} \mathbf{0} & \Psi(\bar{y}) \end{bmatrix} \left(q_\infty \mathbf{K}^{-1} - q_\infty^2 \mathbf{K}^{-1} \frac{\mathbf{K}_a}{q_\infty} \mathbf{K}^{-1} + q_\infty^3 \mathbf{K}^{-1} \frac{\mathbf{K}_a}{q_\infty} \mathbf{K}^{-1} \frac{\mathbf{K}_a}{q_\infty} \mathbf{K}^{-1} \right) \left(\frac{\mathbf{F}_\alpha}{q_\infty} \alpha + \frac{\mathbf{F}_0}{q_\infty} \right) \tag{21}$$

The flexible wing lift coefficient C_L and the rigid wing lift coefficient C_L^* are related by aeroelasticity according to

$$C_L = C_L^* + \frac{2}{S} \int_0^L c_{L\alpha}^* \left[\left(\Theta_\alpha \cos\Lambda - \frac{\partial W_\alpha}{\partial \bar{y}} \sin\Lambda \right) \alpha + \Theta_0 \cos\Lambda - \frac{\partial W_0}{\partial \bar{y}} \sin\Lambda \right] c \cos\Lambda d\bar{y} \tag{22}$$

Then, the flexible wing lift curve slope is related to the rigid wing lift curve slope by the expression

$$C_{L\alpha} = C_{L\alpha}^* + \frac{2}{S} \int_0^L c_{L\alpha}^* \left(\Theta_\alpha \cos\Lambda - \frac{\partial W_\alpha}{\partial \bar{y}} \sin\Lambda \right) c \cos\Lambda d\bar{y} \tag{23}$$

Similarly, the lift coefficient at zero angle of attack for the flexible wing is related to that for the rigid wing by the expression

$$C_{L_0} = C_{L_0}^* + \frac{2}{S} \int_0^L c_{L\alpha}^* \left(\Theta_0 \cos\Lambda - \frac{\partial W_0}{\partial \bar{y}} \sin\Lambda \right) c \cos\Lambda d\bar{y} \tag{24}$$

For sweptback wings, $C_{L\alpha}$ is generally less than $C_{L\alpha}^*$. For an elliptical lift distribution, it can be shown that $c_{L\alpha}^* = C_{L\alpha}^*$ is a constant due to the uniform downwash. So $C_{L\alpha}^*$ can be computed from $C_{L\alpha}$ as

$$C_{L\alpha}^* = \frac{C_{L\alpha}}{1 + \frac{2}{S} \int_0^L \left(\Theta_\alpha \cos\Lambda - \frac{\partial W_\alpha}{\partial \bar{y}} \sin\Lambda \right) c \cos\Lambda d\bar{y}} \tag{25}$$

It is noted that the aeroelastic analysis above is based on linear aerodynamic theory. At a stall angle of attack, the aerodynamic characteristic is nonlinear. So a nonlinear aeroelastic analysis will be required for detail analysis of the aeroelastic effect on $C_{L_{max}}$.

At a constant angle of attack, the wing bending deflection and torsional twist increase with the dynamic pressure. This causes lift to decrease with the dynamic pressure, as observed in the cruise configuration test in 2013.[7] Thus, the aeroelastic effect offsets the Reynolds number effect which causes lift to increase with the dynamic pressure. At α_{stall} corresponding to $C_{L_{max}}$, the Reynolds number effect is apparently more dominant than the aeroelastic effect. At lower angles of attack, the aeroelastic effect is evident as shown in Fig. 35 which shows the C_L at $\alpha = 4^\circ$ for the high-lift configuration HLF1+FLAP1+VCK1.4 actually decreases with the dynamic pressure above 3 psf.

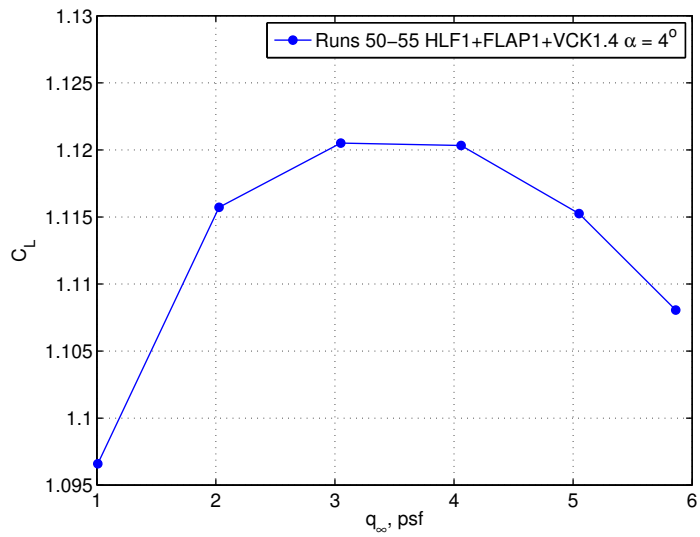

Figure 35. Reynolds Number Effect and Aeroelastic Effect on C_L

Aeroelastic corrections will be required to estimate the aeroelastic effect on $C_{L_{max}}$ for a full-scale configuration in addition to the Reynolds number and Mach number corrections. The bending deflection of a full-scale configuration is expressed as

$$W_f(\bar{y}) = \begin{bmatrix} \Phi(\bar{y}) & \mathbf{0} \end{bmatrix} \left(\mathbf{K}_f + q_{\infty,f} \frac{\mathbf{K}_{a,f}}{q_\infty} \right)^{-1} q_{\infty,f} \frac{\mathbf{F}_f}{q_\infty} \tag{26}$$

where the subscript f denotes the full-scale configuration and $\mathbf{F}_f$ is the generalized aerodynamic force vector of the full-scale configuration.

In contrast, the bending deflection of the wind tunnel model is

$$W(\bar{y}) = \begin{bmatrix} \Phi(\bar{y}) & \mathbf{0} \end{bmatrix} \left(\mathbf{K} + q_\infty \frac{\mathbf{K}_a}{q_\infty} \right)^{-1} q_\infty \frac{\mathbf{F}}{q_\infty} \tag{27}$$

Then the lift coefficient C_{L_f} for the full-scale configuration can be estimated as

$$C_{L_f} = C_L - \frac{2}{S} \int_0^L c^*_{L\alpha} \left(\Theta \cos\Lambda - \frac{\partial W}{\partial \bar{y}} \sin\Lambda \right) c \cos\Lambda d\bar{y} + \frac{2}{S_f} \int_0^{L_f} c^*_{L\alpha} \left(\Theta_f \cos\Lambda - \frac{\partial W_f}{\partial \bar{y}} \sin\Lambda \right) c_f \cos\Lambda d\bar{y}_f \tag{28}$$

This equation can be non-dimensionalized as

$$C_{L_f} = C_L - \frac{b\bar{c}}{S} \int_0^1 c^*_{L\alpha} \left(\Theta \cos\Lambda - \frac{\partial W^*}{\partial \bar{y}^*} \sin\Lambda \right) \frac{c}{\bar{c}} d\bar{y}^* + \frac{b_f \bar{c}_f}{S_f} \int_0^1 c^*_{L\alpha} \left(\Theta_f \cos\Lambda - \frac{\partial W^*_f}{\partial \bar{y}^*_f} \sin\Lambda \right) \frac{c_f}{\bar{c}_f} d\bar{y}^*_f \tag{29}$$

where $\bar{y}^* = \frac{\bar{y}}{L}$, $\bar{y}^*_f = \frac{\bar{y}_f}{L_f}$, $W^* = \frac{W}{L}$, and $W^*_f = \frac{W_f}{L_f}$.

If the wind tunnel model is scaled geometrically using the same scaling factor throughout, then $\frac{b\bar{c}}{S} = \frac{b_f \bar{c}_f}{S_f}$ and $\frac{c}{\bar{c}} = \frac{c_f}{\bar{c}_f}$. Assuming $c^*_{L\alpha}(\bar{y})$ is the same between the full-scale configuration and the wind tunnel model, then the

aeroelastic correction for the lift coefficient only depends on the change in the normalized wing shape given by the following formula:

$$C_{L_f} = C_L + \frac{b\bar{c}}{S}\int_0^1 c_{L\alpha}^* \left[\left(\Theta_f - \Theta\right)\cos\Lambda - \frac{\partial\left(W_f^* - W^*\right)}{\partial \bar{y}^*}\sin\Lambda \right] \frac{c}{\bar{c}} d\bar{y}^* \tag{30}$$

The aeroelastic correction is zero if the normalized wing shape is the same between the full-scale configuration and the wind tunnel model. This would require proper stiffness scaling.

Aeroelastic deflection measurements were taken with the VICON motion tracking system. The VICON system uses optical targets, called dots, to create a three-dimensional displacement field of the wind tunnel model as it is under load. Figure 36 is a schematic diagram of the wind tunnel model showing the VICON measurement points.

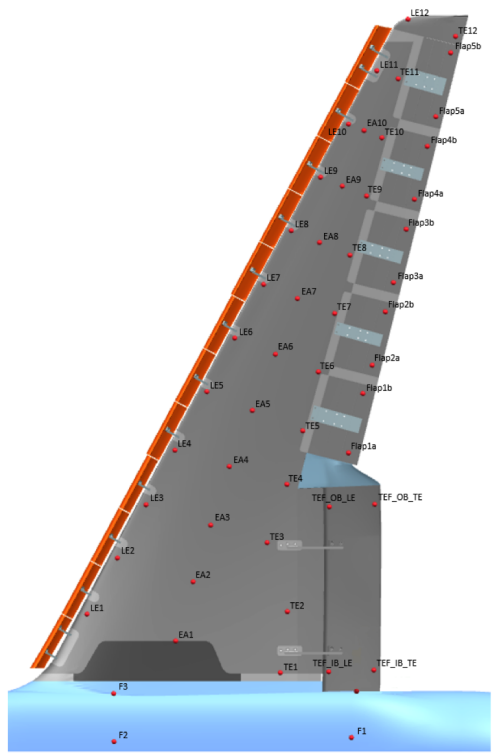

Figure 36. Optical Displacement Measurement Points on Wind Tunnel Model (Courtesy of University of Washington Aeronautical Laboratory)

The bending deflections and torsional twists of the wind tunnel model for run 55 for the high-lift plain flap configuration HLF1+FLAP1+VCK1.4 and run 58 for the high-lift cambered flap configuration HLF2+FLAP1+VCK1.4 at $q_\infty = 5.8$ psf are shown in Figs. 37(a) and (b), respectively. The bending deflections for the two runs are very similar but there appears to be a small offset between the two bending deflections. The torsional twists are not consistent across the wing span. This is because the torsional twists are not directly measured but rather are computed from the displacements measured at the leading edge and trailing edge. The difference between the two numbers is typically very small. Thus, the computed the torsional twists are not expected to be as reliable as the bending deflections. The largest torsional twist is about 1.2° leading edge up, indicating that the lift contribution to the pitching moment is larger than the pitching moment at the aerodynamic center.

The continuous bending deflection can be reconstructed from the bending deflection measurements by the following modal correlation method:[7]

$$W\left(\bar{y}\right) = \Phi\left(\bar{y}\right)\left[\Phi^\top\left(\bar{y}_i\right)\Phi\left(\bar{y}_i\right)\right]^{-1}\Phi^\top\left(\bar{y}_i\right)\mathbf{w} \tag{31}$$

where $\mathbf{w}$ is a vector of the measured bending deflections at $\bar{y} = \bar{y}_i$, and $\Phi^\top\left(\bar{y}_i\right) = \left[\begin{array}{cccc} \Phi^\top\left(\bar{y}_1\right) & \Phi^\top\left(\bar{y}_2\right) & \cdots & \Phi^\top\left(\bar{y}_n\right) \end{array}\right]$.

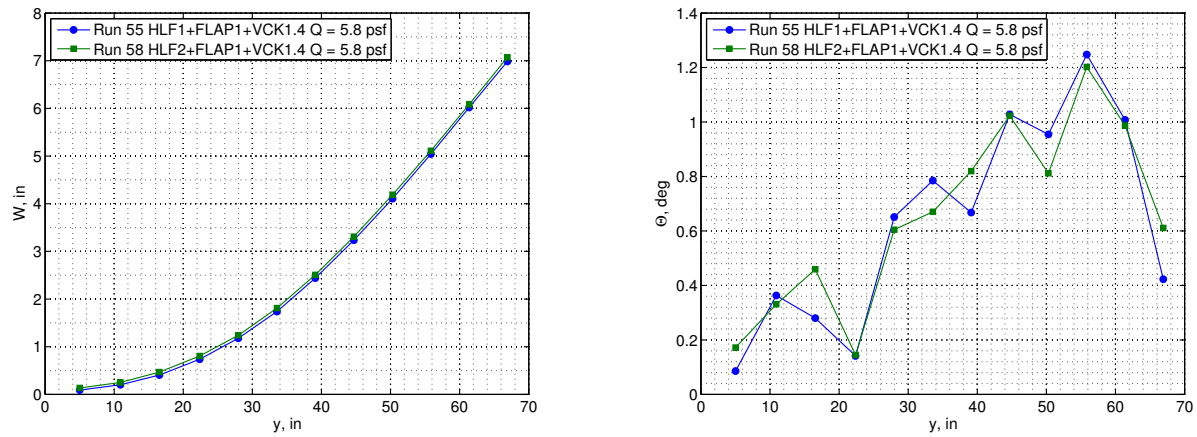

(a) (b)

Figure 37. VICON Measured Bending Deflection and Computed Torsional Twist

The advantage of computing the continuous bending deflection using the modal correlation is that it is based on orthogonal mode shape functions which properly account for structural dynamics of the flexible wing with proper boundary conditions. Therefore, the bending slope can be evaluated analytically from the mode shape derivatives as opposed to by a finite-difference method which can cause inaccuracy. Furthermore, numerical integration can be performed more accurately.

The bending slope is computed as

$$\frac{\partial W(\bar{y})}{\partial \bar{y}} = \frac{\partial \Phi(\bar{y})}{\partial \bar{y}} \left[\Phi^{\top}(\bar{y}_i)\,\Phi(\bar{y}_i)\right]^{-1} \Phi^{\top}(\bar{y}_i)\,\mathbf{w} \tag{32}$$

Similarly, the continuous torsional twist can be approximated by

$$\Theta(\bar{y}) = \Psi(\bar{y}) \left[\Psi^{\top}(\bar{y}_i)\,\Psi(\bar{y}_i)\right]^{-1} \Psi^{\top}(\bar{y}_i)\,\theta \tag{33}$$

where θ is a vector of the computed torsional twists from the VICON measurements.

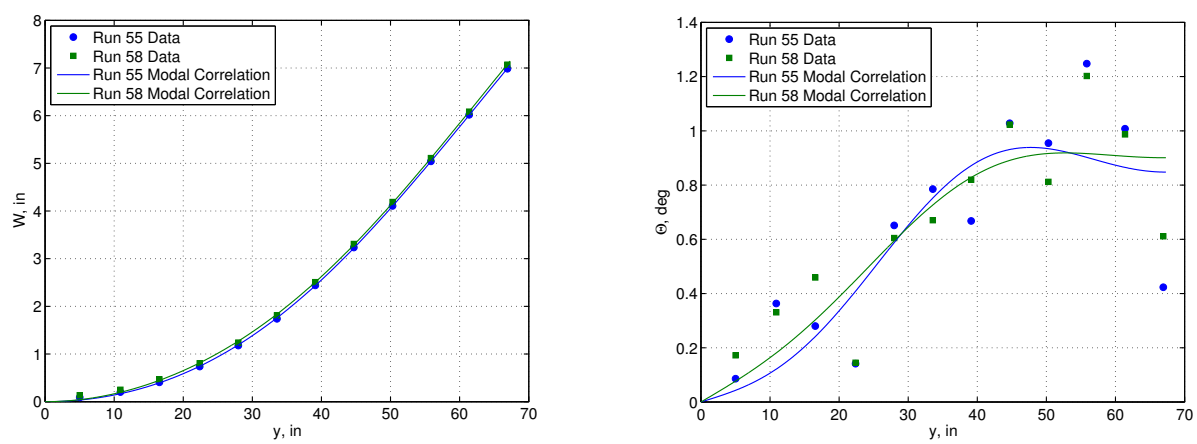

(a) (b)

Figure 38. Modal Correlation of Bending Deflection and Torsional Twist

Figures 38(a) and (b) are the continuous bending deflection and torsional twist computed by the modal correlation using the first three mode shapes of a cantilever beam and a fixed-free torsion rod. Table 3 shows the modal correlation of the bending deflection and torsional twist. The bending deflection has a better modal correlation, as shown by the

decrease in the modal contribution as the order of the mode shape increases. The modal contributions to both the bending deflection and torsional twist are primarily due to the respective fundamental mode shapes.

	Run 55	Run 58
W_1, in	3.2180	3.2747
W_2, in	−0.2929	−0.2655
W_3, in	0.0190	0.0325
Θ_1, deg	0.6769	0.6826
Θ_2, deg	−0.0065	−0.0002
Θ_3, deg	−0.0840	−0.0459

Table 3. Modal Correlation of Runs 55 and 58

Using the functions $W(\bar{y})$ and $\Theta(\bar{y})$, one can estimate the rigid wing lift coefficient C_L^*. Figures 39(a) and (b) are the estimated wash-out twist derivatives of $\frac{\partial W(\bar{y})}{\partial \bar{y}} \sin\Lambda$, $\Theta(\bar{y})\cos\Lambda$, and $\alpha_e(\bar{y})$ with respect to α. Using the previous data points of runs 55 and 58 from the $C_{L_{max}}$ data points, C_{L_α} and C_{L_0} are estimated using an assumption of an effective linear lift curve, which is not strictly correct but may be used as an approximation. Table 4 shows the results of the rigid wing lift coefficient calculation for runs 55 and 58. The rigid wing lift coefficient for run 50 is estimated to be only 1.2% higher than the flexible wing lift coefficient. On the other hand, the rigid wing lift coefficient for run 58 is actually slightly lower than the flexible wing lift coefficient by 0.2%. In theory, as a stall is approached, lift decreases until the lift curve slope is zero, at which point the effect of aeroelasticity becomes small. Note that even though the lift curve slope of a wing may be near zero, the local section lift curve slope can vary significantly. Thus, the effect of aeroelasticity always exists even at a stall condition.

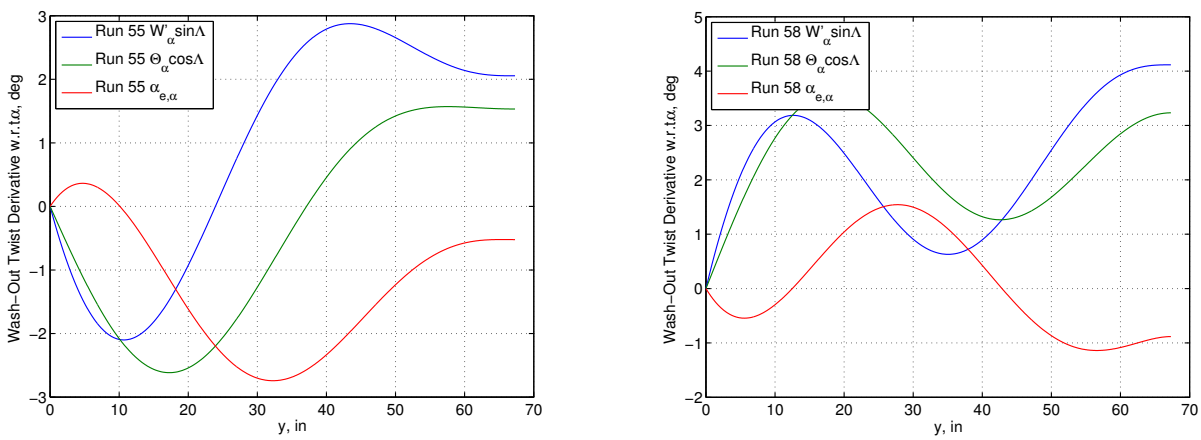

(a) (b)

Figure 39. Wash-Out Twist Derivatives with respect to α for Runs 55 and 58 Computed by Modal Correlation

	Run 55	Run 58
α	20.444°	20.421°
C_L	2.1307	2.0876
C_{L_α}	1.4566	2.1193
C_{L_0}	1.6109	1.3323
$C^*_{L_\alpha}$	1.4811	2.1140
$C^*_{L_0}$	1.6274	1.3297
C^*_L	2.1559	2.0832

Table 4. Estimated Rigid Wing Lift Coefficients of Runs 55 and 58

VII. Conclusions

This paper presents wind tunnel experimental results of a flexible wing high-lift configuration with a variable camber continuous trailing edge flap (VCCTEF) design, tested at the University of Washington Aeronautical Laboratory (UWAL) in July of 2014. The wing structural stiffness in bending is tailored to be half of the stiffness of a Boeing 757-era transport wing, while the torsional stiffness is about the same. This stiffness reduction results in a wing tip deflection of about 10% of the wing semi-span at 1-g flight conditions. The VCCTEF high-lift design does not have a Fowler slot between the main wing and the flap. The high-lift design also includes a Variable Camber Krueger (VCK) leading edge device and an inboard high-lift trailing edge flap with a Fowler motion. The baseline VCK was rigged at 65° uniformly across the wing span based on a two-dimensional CFD analysis. A premature flow separation associated with the VCK leading edge device, as indicated by an abrupt stall, was encountered during the initial runs. Flow control methods using vortex generators and boundary layer trip dots were applied but did not produce a desired effect. It was found that changing the VCK rigging angle has a much greater effect. A final VCK configuration was found experimentally with a varying rigging angle from 65° at the inboard to 50° at the outboard.

Wind tunnel test results indicate a $C_{L_{max}} = 2.13$ is achieved for a wing-body configuration with the single-element plain flap versus $C_{L_{max}} = 2.09$ with the cambered flap. The high-lift $C_{L_{max}}$ is close to the desired $C_{L_{max}}$ for a typical Boeing 757 landing configuration. The wind tunnel test thus confirms that the high-lift design for the VCCTEF is capable of providing high-lift performance for transport aircraft. The cambered flap was found to have a higher L/D by 6% over the single-element plain flap due to the reduced profile drag associated with the cambered flap. The test results thus also confirm the potential drag reduction benefit for the three-segment cambered flap as compared to the plain flap.

Sensitivities of $C_{L_{max}}$ to the VCCTEF spanwise deflection shapes, Fowler slot width, and Reynolds number / aeroelastic effect were studied. 2% Variations in $C_{L_{max}}$ and L/D were noted among four different VCCTEF spanwise deflection shapes with uniform spanwise deflection achieving the highest $C_{L_{max}}$ but also the lowest L/D. Test results for various Fowler gaps ranging from 0.25 inch (baseline) to 0.5 inch show that $C_{L_{max}}$ slightly increases with the Fowler slot width. Because the wind tunnel is an aeroelastic model with a significant aeroelastic deflection, the typical Reynolds number effect and aeroelastic effect act in a combined fashion to produce the sensitivity of $C_{L_{max}}$ to the dynamic pressure. Test results show increasing $C_{L_{max}}$ and decreasing C_D with increasing Reynolds number, as normally expected for a stiff wind tunnel model. This suggests that the Reynolds number effect outweighs the aeroelastic effect at stall. Reynolds and Mach number corrections were performed to estimate the values of $C_{L_{max}}$ at flight Reynolds and Mach numbers. The corrections result in estimated $C_{L_{max}} = 2.22$ for the plain flap and $C_{L_{max}} = 2.19$ for the cambered flap, roughly about 4% increase.

An aeroelastic analysis was performed to analyze the bending deflection measurements from an optical VICON system and the torsional twist data computed from the VICON measurements. The bending deflection measurements show very good data consistency, but the computed torsional twist data exhibit high degree of scatter are are not considered reliable. An aeroelastic correction method for lift is derived and shows that the lift correction only depends on the wing aeroelastic deflection shape. A rigid wing lift coefficient $C_{L_{max}}$ is estimated. The difference between the flexible wing $C_{L_{max}}$ and rigid wing $C_{L_{max}}$ is small because the aeroelastic effect is strongly dependent on the lift curve slope which tends to zero at a stall angle of attack. A nonlinear aeroelastic analysis will be required for analyzing aerodynamic stall.

In summary, the objective of the high-lift wind tunnel test was met and the test results support the high-lift capability of the VCCTEF as a viable concept for a high-lift system.

Acknowledgment

The authors would like to thank the Advanced Air Transport Technology Project under the Advanced Air Vehicles Program of the NASA Aeronautics Research Mission Directorate (ARMD) for funding support of this work. The authors also would like to acknowledge Boeing Research and Technology and the University of Washington for their collaboration with NASA under NASA contract NNL11AA05B task order NNL12AD09T entitled "Development of Variable Camber Continuous Trailing Edge Flap System for B757 Configured with a More Flexible Wing."

References

[1]Nguyen, N., "Elastically Shaped Future Air Vehicle Concept," NASA Innovation Fund Award 2010 Report, October 2010, Submitted to NASA Innovative Partnerships Program.

[2]Nguyen, N., Trinh, K., Reynolds, K., Kless, J., Aftosmis, M., Urnes, J., and Ippolito, C., "Elastically Shaped Wing Optimization and Aircraft Concept for Improved Cruise Efficiency," AIAA Aerospace Sciences Meeting, AIAA-2013-0141, January 2013.

[3]Boeing Report No. 2012X0015, "Development of Variable Camber Continuous Trailing Edge Flap System," October 4, 2012.

[4]Urnes, J., Nguyen, N., Ippolito, C., Totah, J., Trinh, K., and Ting, E., "A Mission Adaptive Variable Camber Flap Control System to Optimize High Lift and Cruise Lift to Drag Ratios of Future N+3 Transport Aircraft," AIAA Aerospace Sciences Meeting, AIAA-2013-0214, January 2013.

[5]Boeing Report No. 2014X0030, "Development of Variable Camber Continuous Trailing Edge Flap System for B757 Configured with a More Flexible Wing," Submitted to NASA, September 27, 2014.

[6]Jordan, T. L., Langford, W. M., Belcastro, C. M., Foster, J. M., Shah, G. H., Howland, G., and Kidd, R., "Development of a Dynamically Scaled Generic Transport Model Testbed for Flight Research Experiments," AUVSI Unmanned Unlimited, Arlington, VA, 2004.

[7]Nguyen, N., Precup, N., Urnes, J., Nelson, C., Lebofsky, S., Ting, E., and Livne, E., "Experimental Investigation of a Flexible Wing with a Variable Camber Continuous Trailing Edge Flap Design," 32nd AIAA Applied Aerodynamics, AIAA 2014-2441, June 2014.

[8]Precup, N., Mor, M., and Livne, E., "Design, Construction, and Tests of an Aeroelastic Wind Tunnel Model of a Variable Camber Continuous Trailing Edge Flap (VCCTEF) Concept Wing," 32nd AIAA Applied Aerodynamics Conference, AIAA-2014-2442, June 2014.

[9]Nguyen, N., Ting, E., and Lebofsky, S., "Aeroelastic Analysis of Wind Tunnel Test Data of a Flexible Wing with a Variable Camber Continuous Trailing Edge Flap (VCCTEF)," 56th AIAA/ASME/ASCE/AHS/SC Structures, Structural Dynamics, and Materials Conference, January 2015.

[10]VICON Website, http://www.vicon.com.

[11]Precup, N., Mor, M., and Livne, E., "The Design, Construction, and Tests of a Concept Aeroelastic Wind Tunnel Model of a High-Lift Variable Camber Continuous Trailing Edge Flap (HL-VCCTEF) Wing Configuration," 56th AIAA/ASCE/AHS/ASC Structures, Structural Dynamics, and Materials Conference, AIAA-2015-1406, January 2015.

[12]NASA OVERFLOW CFD Code Website, http://overflow.larc.nasa.gov.

[13]Buning, P. G., Gomez, R. J., and Scallion, W. I., "CFD Approaches for Simulation of Wing-Body Stage Separation," AIAA- 2004-4838, August 2004.

[14]Spalart, P. R., and Allmaras, S. R., "A One-Equation Turbulence Model for Aerodynamic Flows," AIAA 30th Aerospace Sciences Meeting and Exhibit, AIAA 92-0439, Reno, NV , January 1992.

[15]Yamauchi, G. K. and John, W., "Trends of Reynolds Number Effects on TWQ - Dimensional Airfoil Characteristics for Helicopter Rotor Analyses," NASA TM 84363, April 1983.

[16]Stanford University AA241 Course Website, "Maximum Lift Prediction - Specific Conceptual Design Methods," http://adg.stanford.edu/aa241/highlift/clmaxest.html.

[17]White, F. M., *Viscous Fluid Flow*, McGraw-Hill, Second Edition, 1991.

[18]Bisplinghoff, R. L, Ashley, H., and Halfman, R. L, *Aeroelasticity*, Addison-Wesley, 1955, pp. 478 - 480.